Nanostructured Metal Oxide Thin Films as Photoactive Cathodes of *P*-Type Dye-Sensitised Solar Cells

Danilo Dini

Department of Chemistry, University of Rome ''La Sapienza'', 00139 Rome (Italy)

Abstract

The present review article reports on the recent developments on the determination and analysis of the electrochemical and photoelectrochemical properties of *p*-type semiconducting materials, namely nickel oxide (NiO), prepared with different modalities of deposition and thermal treatment. All these electrodic materials possess a mesoporous morphology as required by the specific application of the dye-sensitized solar cell (DSC), or Grätzel's cell. In particular, NiO thin film electrodes prepared with the methods of screen-printing, spray deposition and sintering under various thermal conditions have been reviewed for the elevated reproducibility of their photoelectrochemical behavior, and the possibility offered by these methods of being scalable. The performance of these electrodes as photoactive cathodes of *p*-DSCs has been compared with the performance of the NiO samples obtained via other methods of sysnthesis/deposition. The choice of the dye sensitizers for *p*-DSCs has been confined to those colorants that have been purposely designed for *p*-type semiconductors, i.e. erythrosine b as benchmark, P1 and perylenemonoimides as highly performing hole photoinjectors, fast green and squaraines. The latter class of dyes is particularly useful for the envisage of tandem DSCs due to their red shifted main absorption with respect to traditional organometallic dye-sensitizers (characteristic of optical complementarity). The recent review of Daeneke *et al.* (ref. 53 in the following) analyzed systematically all the factors influencing negatively the poor performances of *p*-DSCs. They reached the important conclusion that the energy conversion losses of *p*-DSCs were mainly associated to the low fill factors expressed by the *JV* curves of these photoelectrochemical cells. The content of this review differs from that of the work of Daeneke *et al*. since it will be here shown that the photoelectrochemical performances of nanostructured NiO films are heavily determined by the capacitive behavior of NiO. This correlation has been evidenced by the fact that NiO acts as charge storing system in both forward and reverse bias with the retention of ionic charge either on the surface or within the open structure. Adsorption and/or intercalation phenomena in NiO will depend on the nature and size of the ions compensating the electronic charge injected in NiO either electrochemically or photoelectrochemically.

Keywords

Nickel Oxide; DSC; Electrochemistry; P-Type Semiconductor

Introduction

One of the first studies on sensitized *p*-type semiconductors for dye-sensitized solar cells (DSCs) [1] was reported in 1968 by Gerischer *et al.* who proposed the combination of perylene and rhodamine B as *p*-type semiconductor and dye-sensitizer, respectively (**Figure 1**). [2] This seminal work showed photocurrents densities in the order of 10^{-8}- 10^{-7} A cm^{-2}, which have been associated to the photogeneration of mobile electronic deficiencies (holes) in the valence band (VB) of the organic *p*-type system when the latter was polarized as cathode.

The modest performance of such a combination was lately recognized to be a consequence of two main reasons: i) the ill-defined band structure of the aromatic hydrocarbon with separation of the frontier electronic levels that intervene in the process of electron transfer from the *p*-type semiconductor to the redox shuttle through the mediation of the excited dye; ii) the compact morphology of the surface of the organic semiconductor which reduces the surface area of the semiconductor/electrolyte interface. On the other hand, compactness in an organic semiconductor which is in fact a molecular material, is made necessary to allow the effective overlap of molecular orbitals between adjacent conjugated molecules to warrant intermolecular electrical transport. [3] The advent of nanostructured semiconductors of inorganic nature [4] overcame the problem of having incompatibility between open morphology and internal electrical transport. Consequently, DSCs based on nanoporous semiconductors could be exploited successfully for the realization of photoelectrochemical devices with photocurrent densities in

the order of several tens of mA cm^{-2}, and overall conversion efficiencies exceeding 10 %. [5-8] Bulk semiconductors and their nanostructured versions differ mainly for the electronic structure (**Figure 2**), the distribution of the frontier energy levels and charge separation [9]: the most important differences are (i) the decrease of the intrinsic dark conductivity, and (ii) the absence of a built-in electric field in passing from bulk to nanostructured systems. [4]

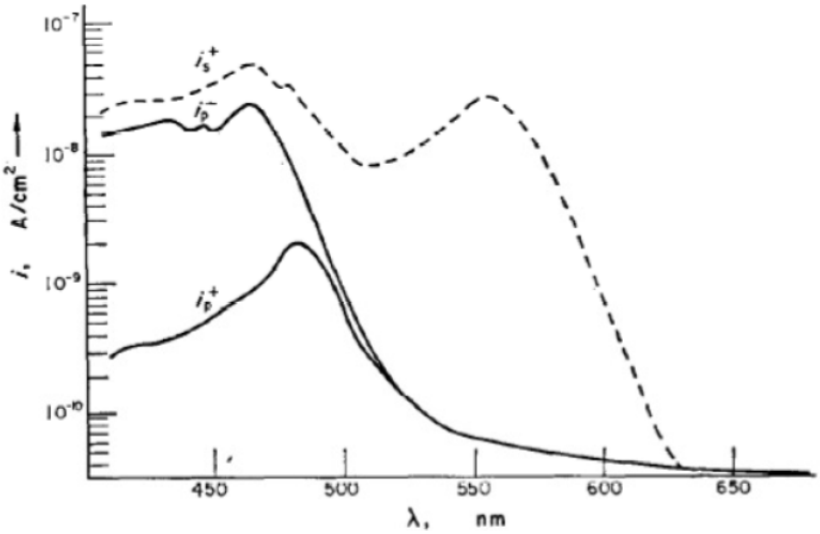

FIGURE 1. PHOTOCURRENT SPECTRUM FOR PERYLENE SINGLE CRYSTAL ELECTRODES IN THE BARE STATE (CURVES WITH SUBSCRIPT P), AND IN THE SENSITIZED STATE WITH RHODAMINE B AS DYE (CURVE WITH SUBSCRIPT S). UPPER-SCRIPTS + AND – REFER TO THE SIGN OF PERYLENE ELECTRODE POLARIZATION. ADAPTED FROM REF. 2.

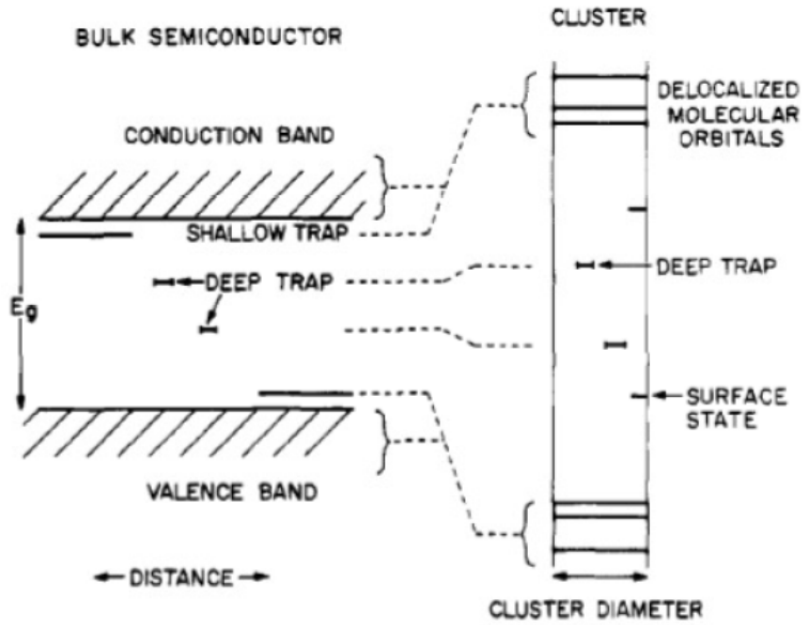

FIGURE 2. DIAGRAM OF CORRELATION BETWEEN THE ELECTRONIC STATES OF A BULK SEMICONDUCTOR AND THE ELECTRONIC STATES OF A SEMICONDUCTING CLUSTER WITH LINEAR SIZES IN THE RANGE 10^1-10^2 Å. ADAPTED FROM REF. 9.

The aspect of the lack of a built-in electric field forces the charge carriers of the nanostructured semiconductors to move through the mesoporous solid exclusively by diffusion, i.e. under a gradient of concentration, and not by migration. This implies that the application of an external bias barely affects the mobility of the charge carriers in nanostructured systems whereas polarization of bulk semiconductors leads to the modification of the width of the space charge layer, and alters the extent of band bending with consequent modification of charge carriers mobility while keeping practically unaltered the surface levels of the bulk semiconductor. [10] The lack of a built-in electric field in nanostructured semiconductors is the consequence of the absence of charge separation within the nanostructure itself due to the actual inexistence of delocalized frontier states. Therefore, the decrease of the electrical conductivity in mesoporous semiconductors can be viewed as a consequence of the lack of frontier molecular orbitals that permeate the whole nanostructured system, and do not allow the extended delocalization of

the electronic charge carriers. With such an electronic structure, the mechanism of charge transport in nanostructured semiconductors is of percolation type and consist in the electron hopping [4] between localized states of defective nature located in interconnected nanocrystallites (random walk). [11] From the energy standpoint, it results that the frontier levels of the nanostructured semiconductors do not form a continuous band as it happens with bulk semiconductors, but are arranged in a set of separated levels that require activation energy for initiating internal charge transport (**Figure 2**). [9] The localized states, associated with shallow and deep traps as well as surface states, are particularly important in nanostructured semiconductors with respect to bulk systems since a relatively high percentage of the interfacial charges that form electrochemical double layer and that define the open circuit potential (V_{OC}) under constant illumination (Eq. 1) can occupy these isolated levels in mesoscopic semiconductors. [12]

$$n = n_0 \cdot exp(eV_{OC}/k_BT) \quad \{1\}$$

In Eq. 1, n is the concentration of free holes when the p-type semiconductor is illuminated, n_0 is the concentration of free holes in dark conditions (equilibrium value), e is the elementary charge, and k_BT is the thermal energy at the given temperature T. In the case of bulk semiconductors, the density of charges occupying these localized states becomes increasingly important only when bulk semiconductor presents irregular structural features (polycrystalline or amorphous solid). [11] For bulk semiconductors of p-type, the characteristic energy level of Fermi ($E_{F,p}$) is calculated through the expression: [13]

$$E_{F,p} = E_{VB} - k_BT \ln(n_h' / N_{VB}') \quad \{2\}$$

in which E_{VB} represents the upper edge of the CB of the p-type semiconductor, n_h' is the density of mobile holes in the VB of the p-type semiconductor (it is expressed in number of holes per cubic centimetre of p-type material), and N_{VB}' is the density of the states available to the holes within the VB (it is expressed as number of electronic states available to the holes in VB per cubic centimetre of p-type material). E_{VB} is evaluated directly through the measurement of the ionization energy of a semiconductor. In first approximation, Eq. 2 can be used also for the definition of the Fermi level of a nanostructured semiconductor provided that the term of density of states per unit energy associated with trap states localized in the bandgap is negligible in the nanostructured system. [14] In Eq.2 the p-type semiconductor is considered in the condition of flat-band potential at which no difference of charge distribution exists between the bulk and the surface of the semiconductor and the energy levels are equalized throughout the different portions of the semiconductor slab (**Figure 3**). [15] Such a depiction of the flat-band condition well describes also the situation of the electronic energy levels in nanostructured semiconductor for which no space charge layer is formed and no charge distribution is then created.

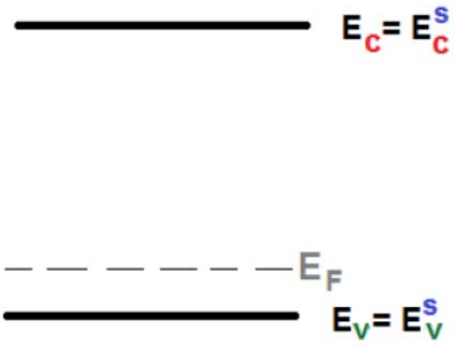

FIGURE 3. DIAGRAM OF FRONTIER ENERGY LEVEL FOR A BULK SEMICONDUCTOR OF *P*-TYPE IN THE CONDITION OF FLATBAND POTENTIAL. E_V, E_V^S, E_C , E_C^S AND E_F REPRESENT THE UPPER EDGE OF THE VALENCE BAND (VB), THE SURFACE ENERGY LEVEL OF THE VB, THE LOWER EDGE OF THE CONDUCTION BAND (CB), THE SURFACE ENERGY LEVEL OF THE CB AND THE FERMI LEVEL, RESPECTIVELY.

Another important difference between bulk and nanostructured semiconductors is related to surface morphology when semiconductors are used as electrodes in an electrochemical cell: nanostructured semiconductor electrodes possess mesoporous surfaces with pores sizes in the order of few nanometers. (**Figures 4-6**) [16-19] The feature of being mesoscopic brings about the increase of the contact area between nanostructured semiconductor and electrolyte of about 1000 times with respect to bulk semiconductors in electrochemical cells having semiconducting

electrodes. This would favour the kinetics of the process of electron transfer (*et*) between the redox species and the nanostructured semiconductor electrode at the electrode/electrolyte interface with consequent increase of the current density (current per electrode unit geometrical area) with respect to bulk systems provided that the same redox process takes place. [20]

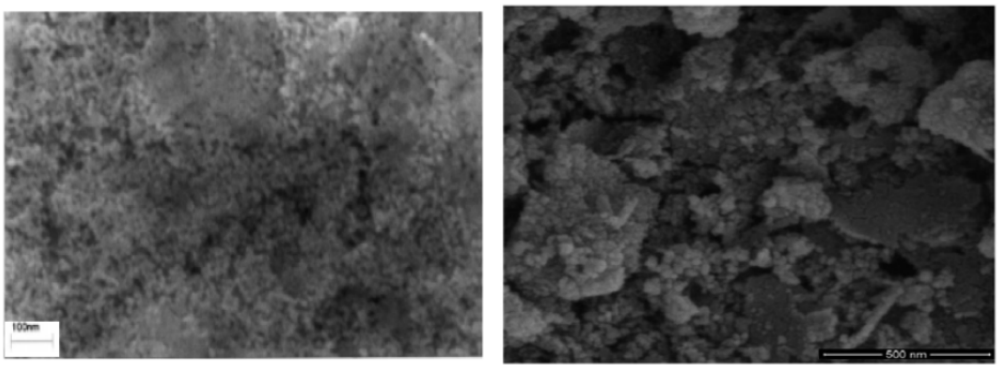

FIGURE 4. (LEFT): SEM IMAGE OF 1 MM THICK FILM OF NIO FOR DSC PURPOSES, WHICH HAS BEEN DEPOSITED VIA SOL-GEL ONTO FLUORINE-DOPED TIN OXIDE (FTO). ADAPTED FROM REF. 16. (RIGHT) SEM IMAGE OF NANOPOROUS NIO PREPARED VIA SPRAY DEPOSITION OF NIO NANOPARTICLES ONTO FTO AND SUCCESSIVELY SINTERED IN PLASMA ATMOSPHERE WITH MICROWAVE RADIATION. ADAPTED FROM REF. 19A.

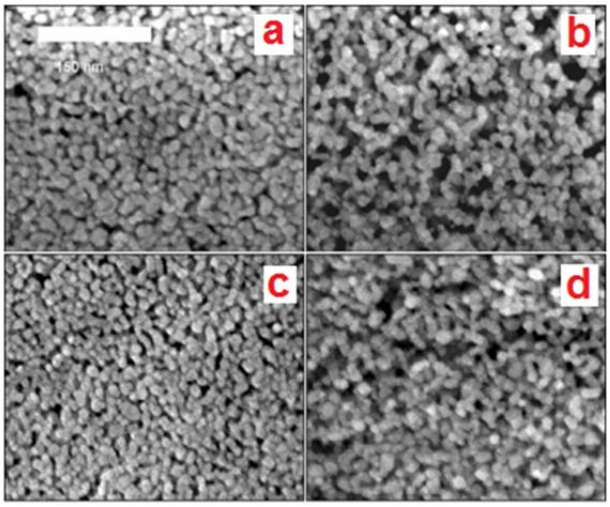

FIGURE 5. FE-SEM IMAGES OF NANOPOROUS NIO FOR DSC PURPOSES DEPOSITED VIA SOL-GEL IN PRESENCE OF NON-IONIC POLYMERIC TEMPLATES. THE FOLLOWING TRIBLOCK CO-POLYMERS HAVE BEEN USED: (A) F88, (B) P105; (C) F108 AND (D) P123. THE ABBREVIATIONS REFER TO DIFFERENT CO-POLYMERIC COMBINATIONS OF PEO AND PPO. ADAPTED FROM REF. 17.

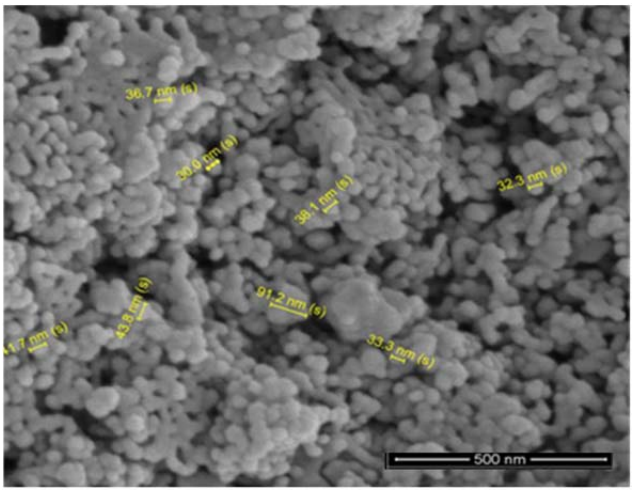

FIGURE 6. SEM IMAGE OF NANOPOROUS NIO PREPARED VIA SPRAY DEPOSITION OF NIO NANOPARTICLES ONTO INDIUM-DOPED TIN OXIDE (ITO) AND SUCCESSIVELY SINTERED IN CONVENTIONAL OVEN. ADAPTED FROM REF. 18.

In order to realize *et* between a *p*-type semiconducting electrode and a redox couple in the electrolyte, the thermodynamic condition to satisfy is the matching of the energy level of the latter with the upper edge of the valence band (VB) of the *p*-type electrode no matter if the semiconducting electrode is nanostructured or not (**Figure 7**).

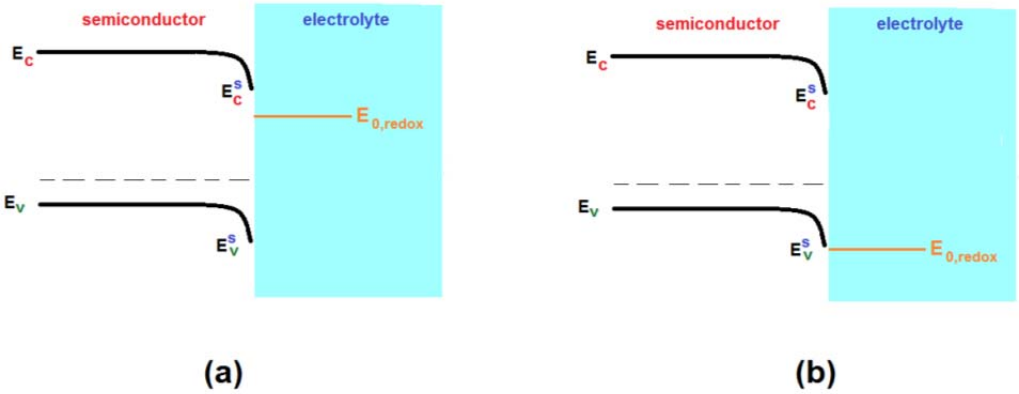

FIGURE 7. SCHEMATIC REPRESENTATION OF THE ENERGY LEVELS AT THE *P*-TYPE SEMICONDUCTOR/ELECTROLYTE INTERFACE INVOLVED IN THE PROCESS OF *ET* WHEN A REDOX COUPLE WITH ENERGY LEVEL E0,REDOX IS PRESENT IN THE ELECTROLYTE. THE *P*-TYPE ELECTRODE IS REVERSE BIASED WITH CONSEQUENT DOWNWARD BENDING OF THE SURFACE ENERGY LEVELS WITH RESPECT TO THOSE OF THE BULK ($E_V > E_V^S$ AND $E_C > E_C^S$). DOTTED LINE REPRESENTS E_F. CASE (A): THE PROCESS OF *ET* OCCURS FROM THE CB OF THE *P*-TYPE ELECTRODE TO THE OXIDIZED FORM OF THE REDOX COUPLE; CASE (B): *ET* OCCURS DIRECTLY FROM THE VB OF THE *P*-TYPE ELECTRODE TO THE OXIDIZED FORM OF THE REDOX COUPLE. IN BOTH CASES (A) AND (B) THE MINORITY CARRIERS OF THE SEMICONDUCTOR, I.E. THE ELECTRONS IN *P*-TYPE SYSTEMS, ARE TRANSFERRED FROM THE ELECTRODE TO THE OXIDIZED FORM OF THE REDOX COUPLE, WHICH, IN TURN, GETS REDUCED. IN CASE OF NANOSTRUCTURED *P*-TYPE SEMICONDUCTORS, THE PHENOMENON OF ENERGY BAND BENDING IS NOT TAKING PLACE.

Mesoporous P-Type Semiconductors

The aspect of the surface area is particularly relevant in the ambit of photoelectrochemical devices like DSCs which are based on nanostructured electrodes. This is because such solar energy conversion devices exploit the large surface area of the nanostructured electrode to anchor very large amounts of dye-sensitizers per unit geometrical area. In *p*-DSCs, dye loadings are typically in the order of 10^{-4} moles per cubic centimetre of porous semiconductor. [21] This brings about the increases of IPCE (incident photon-to-current conversion efficiency) and APCE (absorbed photon-to-current conversion efficiency) values (Eqs. 1 and 2) with respect to bulk semiconductors having a compact morphology. [4]

$$IPCE\ (\lambda) = J_{SC}(\lambda) / e \cdot \varphi(\lambda) = LHE\ \eta_{inj}\ \eta_{coll} \quad \{3\}$$

$$APCE = \frac{IPCE}{LHE} \quad \{4\}$$

LHE being the light harvesting efficiency. LHE is defined as:

$$LHE = 1 - 10^{-A} \quad \{5\}$$

In Eq. 5, the symbol A represents the absorbance of the photoelectrode at a given wavelength. In Eq.3, $J_{SC}(\lambda)$ is the short circuit photocurrent density (in Ampere per square meter) generated by the DSC when this is illuminated with a radiation with wavelength λ, e is the elementary charge, $\varphi(\lambda)$ is the number of incident photons with energy h (c/λ) which impinge the photoelectrode per unit time and unit area (photon flux in photons per second and per square meter of irradiated surface). The term of photon energy contains the symbol c that refers to the speed of light in vacuum. In Eq.3, the two terms of efficiency η_{inj} and η_{coll} indicate the efficiency of charge photoinjection following light absorption, and the efficiency of photocharge collection related to the charge transport through all the electronic conductors (electrodes and external circuit) of the cell, respectively. In terms of mechanism, the charge separation processes following light absorption in sensitized mesoporous semiconductor electrodes immersed in electrolytic solutions occurs at the semiconductor/electrolyte interface and involves transiently populated excited states. The rate of charge separation at the origin of photocurrent in mesoporous based PECs depends on the kinetics of charge injection at this interface and on the relative rate of diffusion of the photoinjected

charges towards the back contact as well as on the rate of recombination (undesired phenomenon). It is therefore particularly important to determine the surface characteristics of the mesoporous semiconductor/electrolyte interface for the evaluation of the transport properties in devices like PECs utilizing nanostructured semiconducting electrodes. [22]

For DSCs, it is found that the highest values of overall conversion efficiencies are prerogative of those devices employing photoactive nanostructured *n*-type semiconductors. [23] Only in relatively recent times researchers got interested in nanostructured *p*-type inorganic semiconductors for DSC purposes either in the single photoactive electrode configuration [24-26] or in the tandem configuration (*t*-DSC). [16,27-29] Performances of *p*-type DSCs (or *p*-DSCs) are comparatively poorer with respect to the *n*-type counterparts, *p*-DSCs efficiencies being typically less than 10% of the best performing *n*-DSC. [30] Historically, the evolution of the *p*-DSCs follows that one of mesoporous nickel oxide (NiO) electrodes since NiO represents the photoactive cathodic material of *p*-DSC par excellence. [31] In fact, except very few cases (e.g. $CuAlO_2$, $CuGaO_2$, $CuCrO_2$ or K_xZnO), [32] the progress on *p*-DSCs is based almost exclusively on the improvement of the methodologies of NiO thin film preparation/deposition, [31, 33] and on the synthesis of optimized dye-sensitizers (**Figure 8**) [34-36] specifically designed to match their HOMO-LUMO levels with the frontier energy levels of nanostructured NiO cathodes (**Figure 9**).

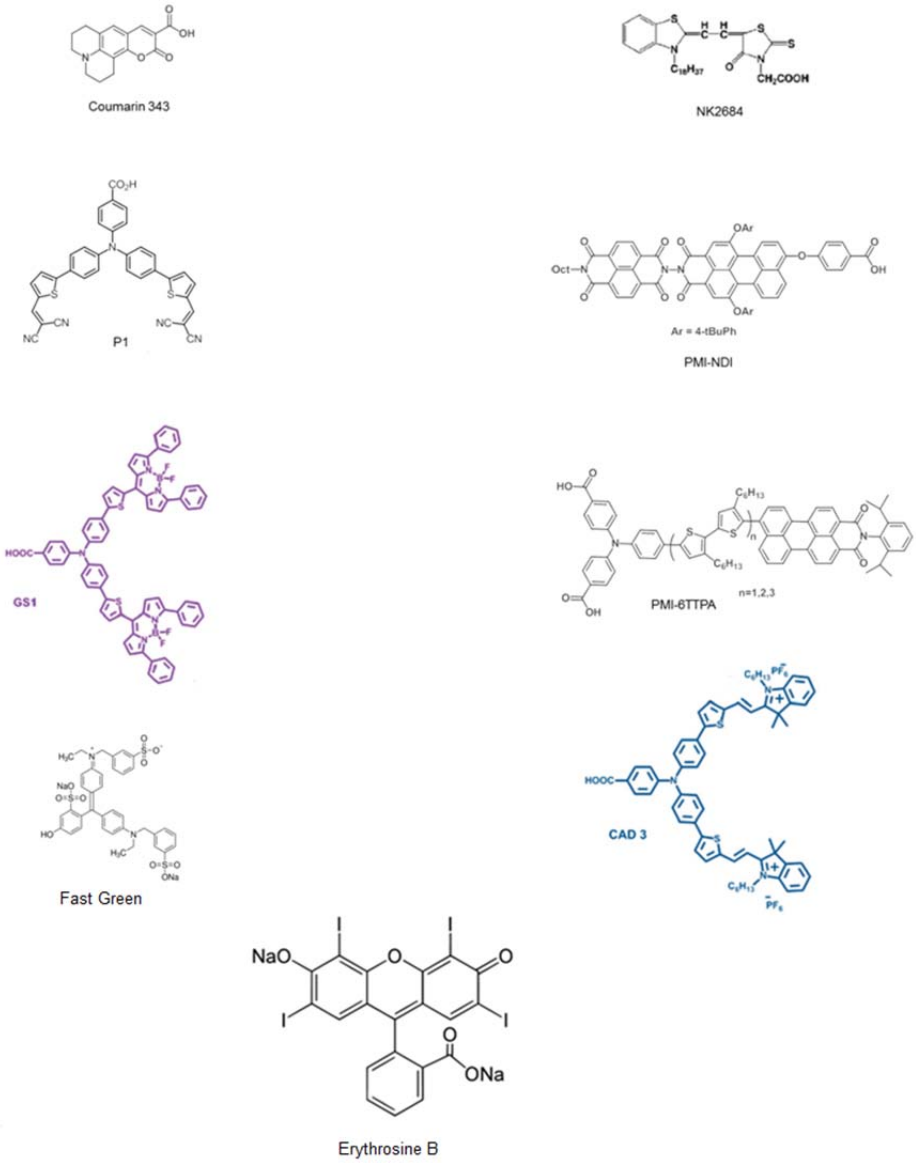

FIGURE 8. MOLECULAR STRUCTURES OF SOME OF THE MOST EFFICIENT DYE-SENSITIZERS USED IN *P*-DSCS WHEN NANOSTRUCTURED NIO IS THE PHOTOACTIVE CATHODE. FOR THIS SET OF COLORANTS, THE MAXIMUM INCIDENT PHOTON-TO-CURRENT CONVERSION EFFICIENCIES (IPCE) OF THE CORRESPONDING *P*-DSCS RANGED BETWEEN 10 AND 65 %. [31, 34]

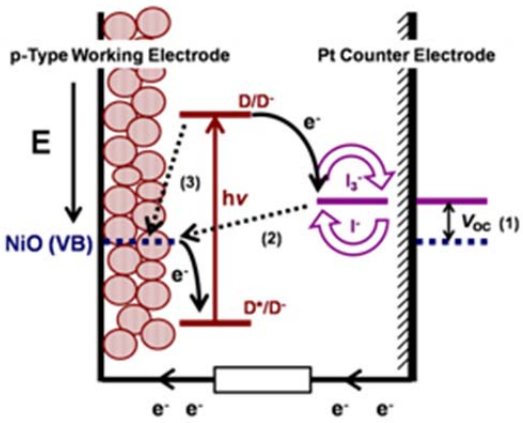

FIGURE 9. SCHEMATIC ILLUSTRATION OF THE OPERATING PRINCIPLE AT THE BASIS OF A *P*-DSC. DOUBLE ARROW (1) REPRESENTS THE POTENTIAL DIFFERENCE BETWEEN THE FERMI LEVEL OF NIO AND THE REDOX COUPLE I_3^-/I^-, WHICH REPRESENTS THE MAXIMUM PHOTOVOLTAGE OF THE DEVICE (V_{OC}). DOTTED ARROWS (2) AND (3) ARE THE TWO MAIN UNDESIRED RECOMBINATION PROCESSES: (2) RECOMBINATION BETWEEN THE REDUCED FORM OF REDOX COUPLE AND NIO, AND (3) BETWEEN THE PHOTOREDUCED DYE (D^-) AND NIO.

The principal motivation at the basis of the development of increasingly efficient *p*-type materials for DSCs is the possibility of achieving theoretical efficiencies about 1.5 times larger for tandem devices utilizing simultaneously both *p*- and *n*-type photoactive electrodes [37-39] with respect to those photoelectrochemical devices employing only one photoactive electrode. [40] When photocathode and photoanode are combined in the same photoelectrochemical cell, the resulting *t*-DSC will generally display a larger open circuit photovoltage (V_{OC}) with respect to the photocells with single photoactive electrode, [16] being approximately V_{OC}(*t*-DSC) = V_{OC}(*p*-DSC) + V_{OC}(*n*-DSC) with V_{OC}(*p*-DSC) and V_{OC}(*n*-DSC) which represent the open circuit voltage of the *p*-DSC having the same cathode of the *t*-DSC, and the open circuit voltage of the *n*-DSC having the same anode of the *t*-DSC, respectively. [41] The most important consequence of such an additive rule for the open circuit potentials of *p*- and *n*-DSCs is the total dependence of V_{OC}(*t*-DSC) on the chemical nature of the two photoactive electrodes (**Figure 10**) and not on the Nernst potential of the redox mediator.

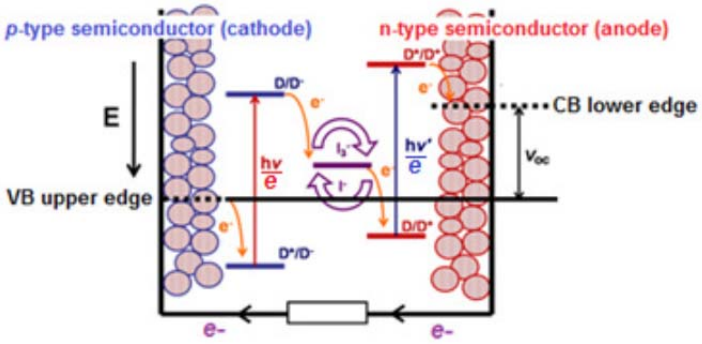

FIGURE 10. POSITION OF THE POTENTIAL (E) LEVELS INVOLVED IN THE *ET* PROCESSES IN A *T*-DSC AND DESCRIPTION OF THE MOVEMENTS OF THE ELECTRONS IN THE DIFFERENT STEPS OF PHOTOCURRENT GENERATION. DYES **D** (THE ANODE SENSITIZER) AND **D** (THE CATHODE SENSITIZER) ARE DIFFERENT, I.E. ABSORB THE RADIATION ENERGY IN DIFFERENT PORTIONS OF THE VISIBLE SPECTRUM ($h\nu$ AND $h\nu'$), AND HAVE BEEN DISTINGUISHED WITH DIFFERENT COLOURS. THE OPEN CIRCUIT POTENTIAL V_{OC} EQUALS PRACTICALLY THE DIFFERENCE BETWEEN THE VB UPPER EDGE OF THE CATHODE (THE POSITIVE POLE OF THE PEC) AND THE CB LOWER EDGE OF THE ANODE (THE NEGATIVE POLE OF THE PEC). THE REDOX MEDIATOR IS REPRESENTED BY THE COUPLE I_3^-/I^-. IN THE EXTERNAL CIRCUIT ELECTRONS FLOW FROM THE ANODE TO THE CATHODE.

The practical rule of the additive property of the open circuit photovoltages of *p*-/*n*-DSCs that combine into the corresponding *t*-DSC does not hold when the parameter of the photocurrent is considered. In case of mismatch between the photocurrents produced singularly by the *n*-DSC and *p*-DSC, the resulting combined *t*-DSC will produce a photocurrent value that is controlled by the less performing photoelectrode. As previously stated, the latter is usually represented by the photocathode, and the photocurrent of the *t*-DSC equals approximately that of the *p*-DSC (**Figure 11**). [42]

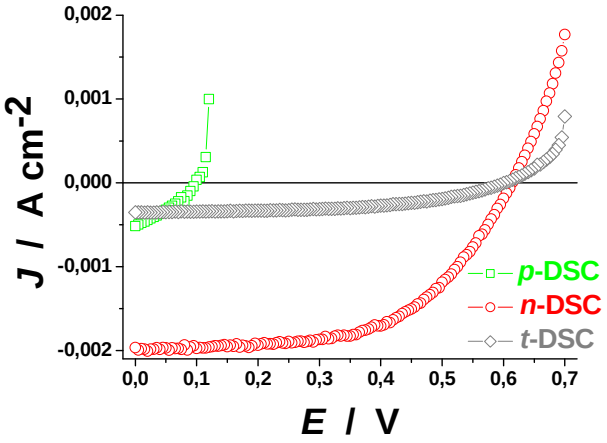

FIGURE 11. CHARACTERISTIC *JV* CURVES OF A *P*-DSC, AN *N*-DSC AND THE *T*-DSC OBTAINED UPON COMBINATION OF THE *P*-DSC PHOTOCATHODE WITH THE *N*-DSC PHOTOANODE. THE *P*-DSC USES NIO ELECTRODE WITH FAST GREEN DYE-SENSITIZER; THE *N*-DSC USES TiO_2 ELECTRODE WITH N-719 DYE-SENSITIZER. REDOX SHUTTLE: I_3^-/I^-. LIGHT SOURCE: SUN SIMULATOR WITH AM 1.5. THE *P*-DSC, *N*-DSC AND *T*-DSC SHOWED OVERALL EFFICIENCIES OF 0.018, 0.692 AND 0.111 %, RESPECTIVELY. FILL FACTORS WERE 35.4, 56.9 AND 51.6 % FOR THE *P*-DSC, *N*-DSC AND *T*-DSC, RESPECTIVELY. THE TANDEM DEVICE WAS ILLUMINATED FROM THE SIDE OF THE PHOTOANODE. ADAPTED FROM REF. 42.

Such a shape of the *JV* curves generated by DSCs is generically described in terms of resistance-like behaviour for a *p-n* junction that represents the system for which the diode equation of the current density has been validated in electronics (Eq.6): [43]

$$J_{photo} = J_{SC\,(ill)} - J_{dark}[exp(qV/mkT) - 1] \quad \{6\}$$

In Eq.6, J_{photo} is the net photocurrent density, $J_{SC\,(ill)}$ is the short-circuit photocurrent density under illumination, J_{dark} is the dark photocurrent density, m is the ideality factor of the diode, V is the voltage difference between the contacts, q is the elementary charge, kT is the thermal energy. The net photocurrent density of a nanostructured DSC is related to its open circuit voltage through the relationship: [43]

$$J_{photo} = J_{SC(ill)} \cdot \{1 - exp[q(V - V_{OC})/mkT]\} / [1 - exp(-qV_{OC}/mkT)] \quad \{7\}$$

It must be here recalled that a DSC is an electrochemical cell and, as a such, differs quite considerably from a single *p-n* junction. This is mainly because of the presence of an electrolyte that transports current via mass and not electron transfer. In fact, the DSC possesses two double layers (and not one like a *p-n* junction) at which charge separation occurs and generates a potential difference between the two electrode/electrolyte interfaces. The build-up of the two electrochemical double layers in the DSC requires mass transfer while the build-up of the potential due to charge separation at the sole interface of a simple *p-n* junction is achieved via electron transfer. This necessarily implies quite substantial differences in the process of double layer build-up for the two distinct types of interfacial systems with the DSC presenting the slowest kinetics of charge separation at its interfaces with respect to a *p-n* junction. Moreover, the electric fields associated to the charged double layers are generally higher in *p-n* junctions in comparison to DSCs. This is a consequence of the closer distances at which charge distributions are separated in the *p-n* junctions for the absence of species solvating the charges at the double layer of a *p-n* junction. This combination of factors requires an analysis of the characteristic *JV* curves for a DSC with nanostructured dyed semiconducting electrodes, [44] which is distinct from the one developed for *p-n* junctions consisting of compact slabs of non-sensitized semiconductors. [45] Another factor of deviation from ideal diode behaviour is the phenomenon of charge storage (*vide infra*) which can take place in mesoporous films with eventual Van der Waals interactions present in the solid.

The overall process that generates the photocurrent in the external circuit of an illuminated *t*-DSC consists of the transfer of electrons from the conduction band (CB) of the anode, i.e. the negative pole of the photoelectrochemical cell (PEC), to the valence band (VB) of the cathode representing the positive pole of the PEC. In the internal circuit of the *t*-DSC, electrons are transferred from the *p*-type cathode to the *n*-type anode by means of a redox process that involves a mediator (or redox shuttle). [46, 47] At the *n*-type anode, the reduced form of the redox mediator gets oxidized and reaches the *p*-type cathode by diffusion. [48] This must occur to restore its initial reduced state and to continue the cycle. In doing so, the passage of the electrical current is warranted also through the electrolyte

of the *t*-DSC. In *t*-DSC, the absorption of the visible portion of the solar radiation provides the energy necessary to create charge separation in the dyes, i.e. the actual visible light absorbing species, which have been immobilized on the surfaces of both PEC electrodes. The initial step of photoinduced charge separation occurs in the dye which has been brought to an excited vibrational-electronic state. This step is followed by charge injection from the excited dye to the electrode on which the dye is chemisorbed. Charge injection from the excited dye-sensitizer to the electrode is energetically possible in both sensitized electrodes of a *t*-DSC. This is because the energy level of the excited electron of a dye-sensitizer is set above the lower threshold of the CB of the *n*-type anode, and collocated above the upper edge of the VB of the *p*-type cathode (**Figure 10**). At the negative electrode of the PEC, electron transfer (*et*) occurs from the highest SOMO level of excited dye to the CB of the *n*-type electrode (**Figure 12**), whereas at the cathode *et* occurs from the VB of the *p*-type electrode to the lowest SOMO level of excited dye (**Figure 13**). In terms of kinetics, the step of *et* between the photoexcited dye and the corresponding supporting electrode can be of two types: fast or slow charge injection with respect to the step of dye regeneration operated by the redox mediator (**Figures 12** and **13**). Dye regeneration consists in an *et* between dye and redox mediator to restore the dye in the electrically neutral form at the electronic ground state. A relatively fast injection [case (b) of **Figures 12** and **13**] will produce a temporary situation in which the chemisorbed dye is charged, i.e. the dye is in a transient oxidized/reduced state. In the case of relatively slow charge injection between excited dye and electrode substrate [case (a) of **Figures 12** and **13**], the excited dye-sensitizer gets back to the electronic ground state following the interaction with the redox mediator without passing through a transient charged state. Depending on the kinetics, the solvent and the supporting electrolyte will have a different influence in stabilizing the transient state of the dye-sensitizer if the latter is neutral or charged. [49]

FIGURE 12. MECHANISM AND ENERGY LEVELS INVOLVED IN THE PROCESS OF ELECTRON TRANSFER FROM THE REDUCED FORM OF THE REDOX MEDIATOR TO THE DYE SENSITIZER IN A *N*-TYPE ANODE OF A *T*-DSC WHEN: (A) THE ELECTRON IS UPTAKEN BY THE DYE IN THE EXCITED STATE AND PRECEDES ELECTRON INJECTION IN THE SEMICONDUCTOR CB (CASE OF SLOW CHARGE INJECTION); (B) THE ELECTRON IS UPTAKEN BY THE DYE IN THE OXIDIZED STATE AND FOLLOWS ELECTRON INJECTION IN THE SEMICONDUCTOR CB (CASE OF FAST CHARGE INJECTION AND SLOW DYE REGENERATION). THE SEPARATION BETWEEN THE HOMO AND LUMO LEVELS OF THE IMMOBILIZED SENSITIZER IS ASSUMED TO BE THE UNVARIED WHEN THE DYE PASSES FROM THE (A) NEUTRAL TO THE (B) OXIDIZED STATE.

FIGURE 13. MECHANISM AND ENERGY LEVELS INVOLVED IN THE PROCESS OF ELECTRON TRANSFER FROM THE DYE SENSITIZER TO THE OXIDIZED FORM OF THE REDOX MEDIATOR IN A *P*-TYPE CATHODE OF A *T*-DSC WHEN: (A) THE ELECTRON IS TRANSFERRED BY THE DYE IN THE EXCITED STATE AND PRECEDES HOLE INJECTION IN THE SEMICONDUCTOR VB (CASE OF SLOW CHARGE INJECTION); (B) THE ELECTRON IS TRANSFERRED BY THE DYE IN THE REDUCED STATE TO THE OXIDIZED FORM OF THE REDOX MEDIATOR AND FOLLOWS HOLE INJECTION IN THE SEMICONDUCTOR VB (CASE OF FAST CHARGE INJECTION AND SLOW DYE REGENERATION). THE SEPARATION BETWEEN THE HOMO AND LUMO LEVELS OF THE IMMOBILIZED SENSITIZER IS ASSUMED TO BE THE UNVARIED WHEN THE DYE PASSES FROM THE (A) NEUTRAL TO THE (B) REDUCED STATE.

The performance of a generic DSC is evaluated by means of the determination of three main parameters, namely J_{SC}, V_{OC}, and the fill factor (FF), which are all related to the overall efficiency η through the relationship:

$$\eta = J_{SC} \cdot V_{OC} \cdot FF / I_{in} \quad \{8\}$$

in which I_{in} represent the total intensity (expressed in W m^{-2} or W cm^{-2}) of the incident radiation. At a given level of illumination, the three relevant parameters of the DSC are dependent on many factors that, in turn, are related to the nature of the materials employed in the PEC, size and geometry of the device, configuration of electrical connections, positioning of the device with respect to the source of illumination as well as to the nature of the radiation source itself. [50] When *p*-DSCs are considered, the highest efficiency reported insofar is 1.67 % with FF of 0.52 when screen-printed NiO is the nanoporous cathode sensitized with PMI-6T-TPA (**Figure 8**), and the illumination source is the artificial sun emitting one tenth of its total power (redox shuttle: $Co(en)_3^{3+}/Co^{2+}$). [51] At highest doses of irradiation (1 sun) the same device drops its efficiency to 1.30 % and FF becomes 0.46 while IPCE exceeds 60 % in the spectral range 400-550 nm. In these conditions, the corresponding kinetic parameter of holes lifetime (τ_h) was 0.66 ms under 1 sun of illumination. The same combination of nanostructured photocathode (in the morphology of microballs, **Figure 14**) and PMI-6T-TPA dye-sensitizer gave a maximum efficiency of 0.46 %, maximum IPCE of 74 % at around 500 nm, with a FF value of 0.34 when the *p*-DSC employed the more common redox shuttle I_3^-/I^-. [52]

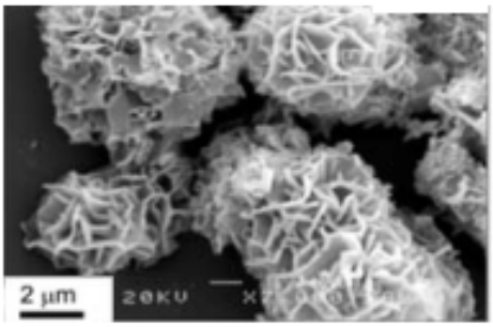

FIGURE 14. SEM IMAGES OF NIO MICROBALLS FOR DSC PURPOSES WHICH HAVE BEEN PREPARED VIA A THERMOLYSIS METHOD. ADAPTED FROM REF. 52.

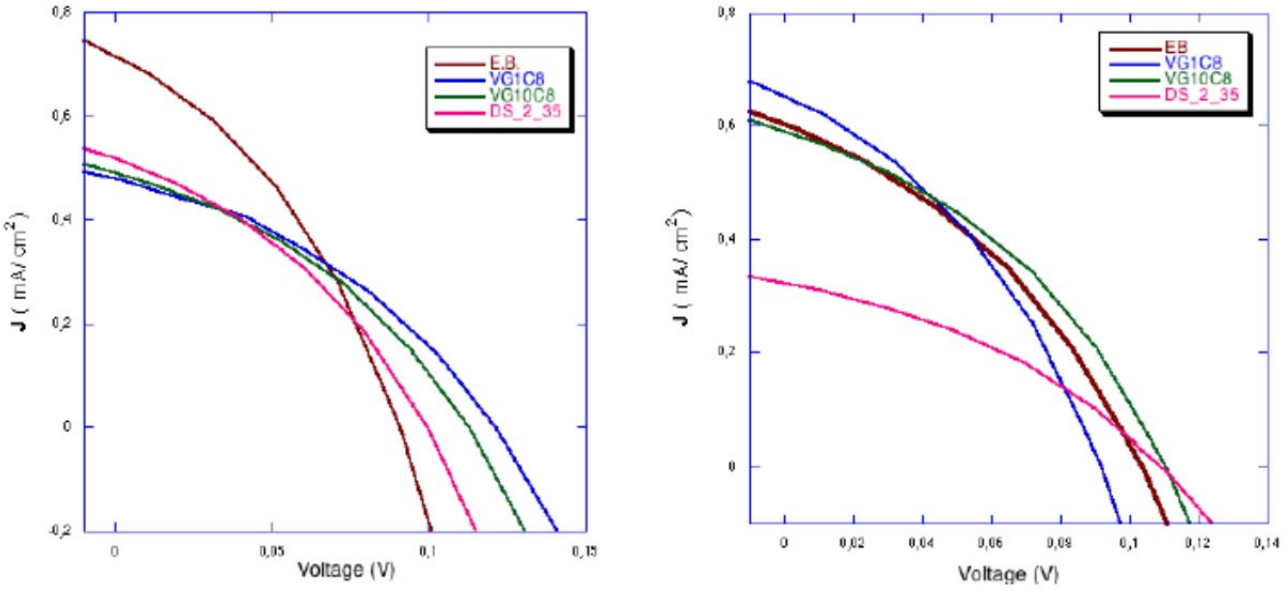

FIGURE 15. CHARACTERISTIC *JV* CURVES OF THE *P*-DSCS UTILIZING THE MESOPOROUS NIO CATHODES OBTAINED VIA SCREEN-PRINTING DEPOSITION OF A VISCOUS DISPERSION OF NIO NANOPARTICLES (DIAMETER: 50 NM; DISPERSANT: ETHYL-CELLULOSE). THE *JV* SHAPES HERE SHOWN PRESENTED LOW FF VALUES (FF < 0.40) DUE MAINLY TO HEAVY RECOMBINATION PROCESSES. DEVICE AREA: 0.25 CM^2; NIO FILM THICKNESS: 4 micron; SENSITIZATION TIME: 16 HRS. EB INDICATES ERYTHROSINE B AS DYE-SENSITIZER (FIGURE 8); VG1C8, VG10C8 AND DS_2_35 INDICATE SYMMETRICAL SQUARAINES WITH AN EVEN NUMBER OF ANCHORING CARBOXYLIC GROUPS. LEFT: AS DEPOSITED NIO CATHODE; RIGHT: ALKALI TREATED NIO CATHODE. ADAPTED FROM REF. 26.

These record values for *p*-DSCs having mesoporous NiO sensitized with organic dyes as photoactive cathode are clearly well below the corresponding values of the best performing *n*-DSCs based on TiO_2 photoanodes sensitized with organometallics. [7] A very recent work of Daeneke *et al.* [53] analyzes and discusses separately all the main factors that are expected to affect negatively the relatively poor performances of NiO based *p*-DSCs. The main conclusion the authors recognize in the low FF is the most important cause of performance impoverishment in *p*-DSCs. [53] This is equivalent to state that upon moving the electrical potential away from the condition of open circuit, the absolute value of the photocurrent density for a *p*-DSC in its discharge process rises very slowly towards the upper limit of short-circuit condition (**Figure 15**). [26]

It is generally acknowledged that the heavy phenomena of recombination occurring in *p*-DSCs are at the basis of the poor performances of this type of PECs as determined by the low fill factors. [43,53] In the case of mesoporous NiO, thin films like those that have been prepared via micelle template, [54] two-step sol-gel, [55] screen printing [26] or plasma sintering, [32] (**Figures 16-19**) the extent of recombination phenomena typical of two-electrode *p*-DSC can be evaluated in three-electrode cells through the determination of the anodic currents associated to the dark oxidation of NiO (either in the bare or a coloured state) when the oxide is in contact with an electrolyte containing the reduced form of the redox shuttle (**Figure 20**). [56] These experimental conditions reproduce electrochemically in the dark the situation of an illuminated sensitized NiO for which holes photoinjection and dye neutralization have already occurred and recombination with the photoreduction product (which can be either I^- or the reduced form of any other appropriate redox shuttle), can then start.

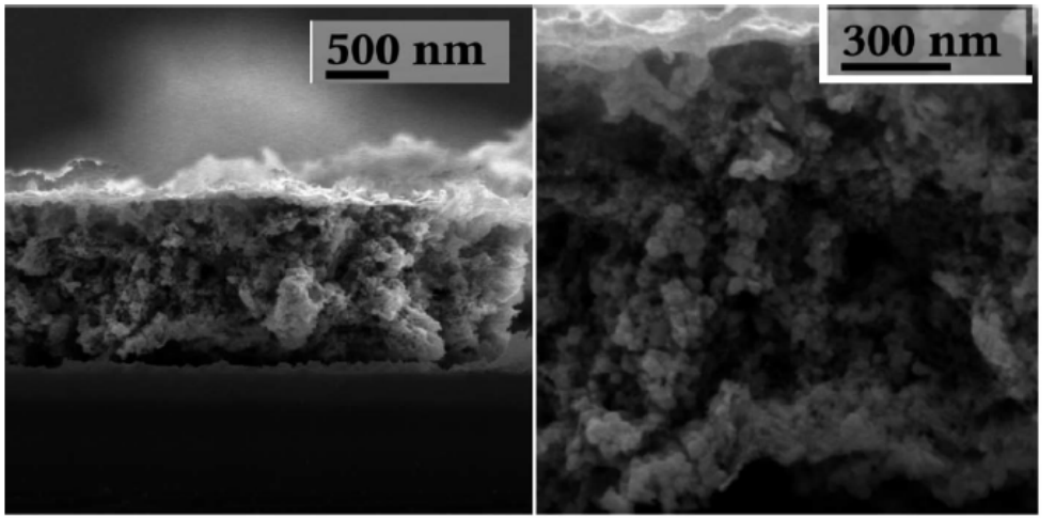

FIGURE 16. SEM IMAGES OF NIO CROSS SECTION AT DIFFERENT MAGNIFICATIONS. METAL OXIDE SAMPLE WAS PREPARED VIA MICELLES FORMATION WITH AMPHIPHILIC POLYSTYRENE- POLY-(2-VINYLPYRIDINE) DIBLOCK COPOLYMERS AS TEMPLATES. ADAPTED FROM REF. 54.

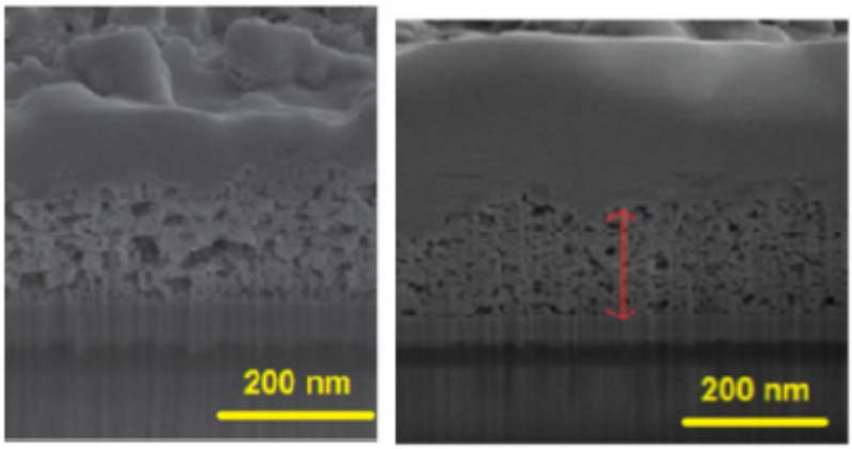

FIGURE 17. SEM IMAGES OF THE CROSS SECTIONS OF NIO DEPOSITED WITH DIFFERENT DEPOSITION TECHNIQUES AND UNDER DIFFERENT PROCESSING CONDITIONS UTILIZING NIO NANOPARTICLES AS PRECURSORS. ADAPTED FROM REF. 32.

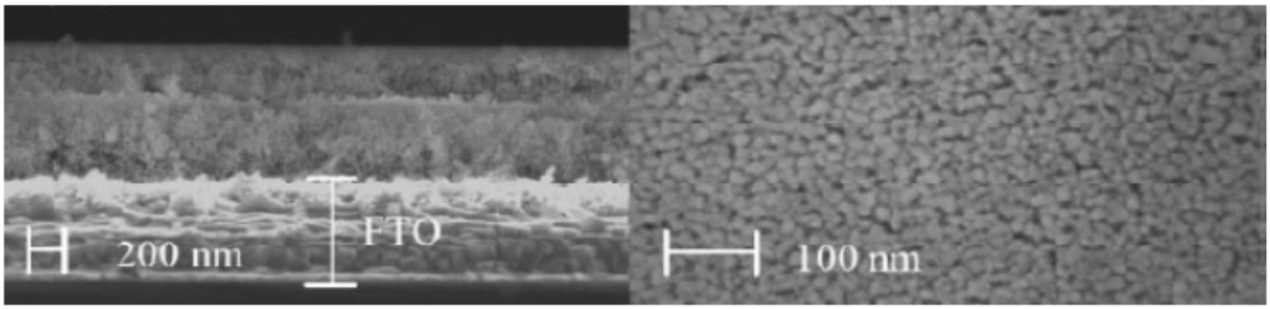

FIGURE 18. SEM IMAGES OF (LEFT) CROSS-SECTION AND (RIGHT) SURFACE OF A NIO FILM PREPARED VIA SOL-GEL IN TWO DISTINCT STEPS. ADAPTED FROM REF. 55.

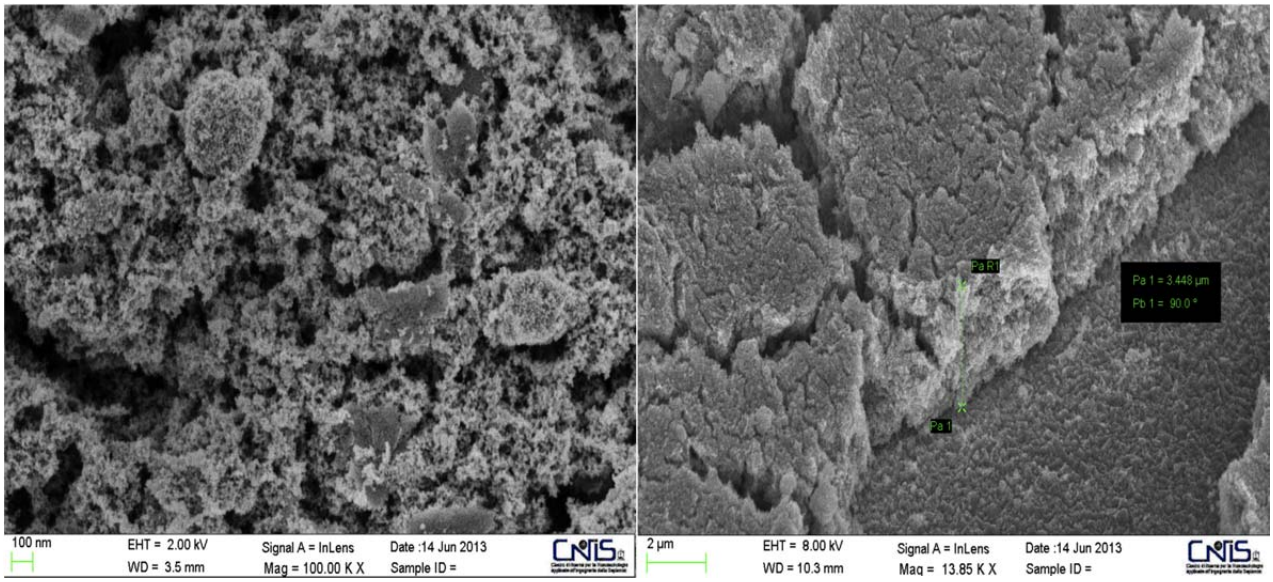

FIGURE 19. FE-SEM IMAGES SHOWING (LEFT) SURFACE MORPHOLOGY AND (RIGHT) CROSS-SECTION OF THE MESOPOROUS NIO ELECTRODE OBTAINED VIA SCREEN-PRINTING OF PREFORMED NIO NANOPARTICLES. ADAPTED FROM REF. 26.

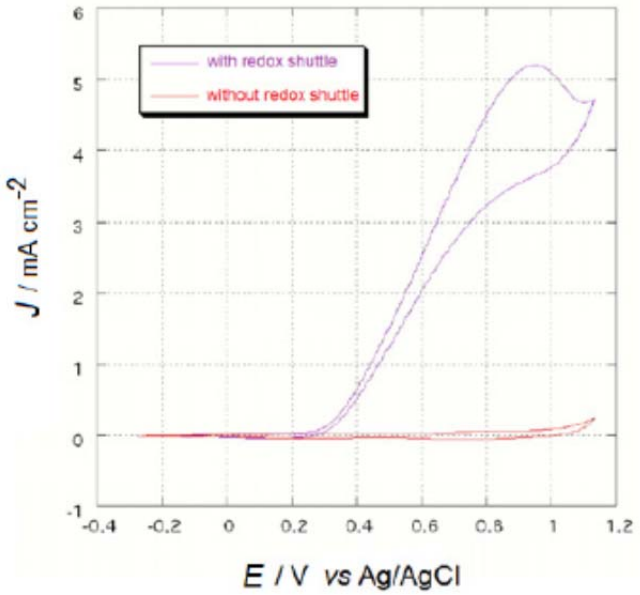

FIGURE 20. DARK VOLTAMMOGRAM OF NIO WITH AND WITHOUT REDOX SHUTTLE. SCAN RATE: 20 MV S^{-1}. ELECTROLYTE COMPOSITIONS WERE 0.2 M $LICLO_4$ IN MPN (RED CURVE) AND 0.2 M I^-/0.02 M I_2 IN MPN (VIOLET CURVE). CONFIGURATION WAS A THREE-ELECTRODE CELL WITH AG/AGCL AS REFERENCE ELECTRODE, AND PT AS COUNTER ELECTRODE. ADAPTED FROM REF. 56.

It was clear that upon dark electrochemical oxidation of mesoporous NiO in the bare state, the oxide layer is prompted to start the oxidation of I^- , i.e. the process of recombination that is induced electrochemically in dark

conditions. [56] The current density exchanged in the process of I^- oxidation results much larger than that produced by the oxidation of sole mesoporous NiO (**Figure 20**). This result indicates how strong is the tendency of the holes localized on NiO surface to recombine with the reduced form of the shuttle especially in the specific case of the recombination with I^-. The latter species can be either adsorbed on electrode surface (especially if the reduced form is of anionic form, like I^-), or localized on the electrolyte side of the electrochemical double layer. In both cases, the kinetics of recombination is of bimolecular nature with a rate depending on the product:

$$v_{rec} = k_{rec}[h^+]_{surf}[I^-]_{surf} \quad \{9\}$$

with $[h^+]_{surf}$, $[I^-]_{surf}$ and k_{rec} representing the surface concentration of the holes injected electrochemically in NiO electrode, the concentration of the reduced form (namely I^- in the present case) at the electrode surface, and the rate constant of electron transfers from I^- to NiO (which constitutes the actual process of recombination), respectively.

The concentration $[h^+]_{surf}$ depends always on the value of the electrical potential of NiO (Eq. 1) either in the dark or under illumination. Anyway, in the latter case the possible presence of a dye-sensitizer on NiO electrode will affect such a potential value in dependence of its efficaciousness to photoinject holes in the oxide upon light excitation of the dye. The recombination between oxidized NiO (on FTO) and I^- is kinetically favoured with respect to the same process occurring on bare FTO (**Figure 21**). It is expected that such an electrocatalytic effect of mesoporous NiO with respect to bare FTO towards the process of I^- oxidation will render unnecessary the deposition of a first compact layer of NiO directly on FTO [57] as preventer of the shunting effect which consists in the oxidative recombination at the uncoated FTO/electrolyte interface.

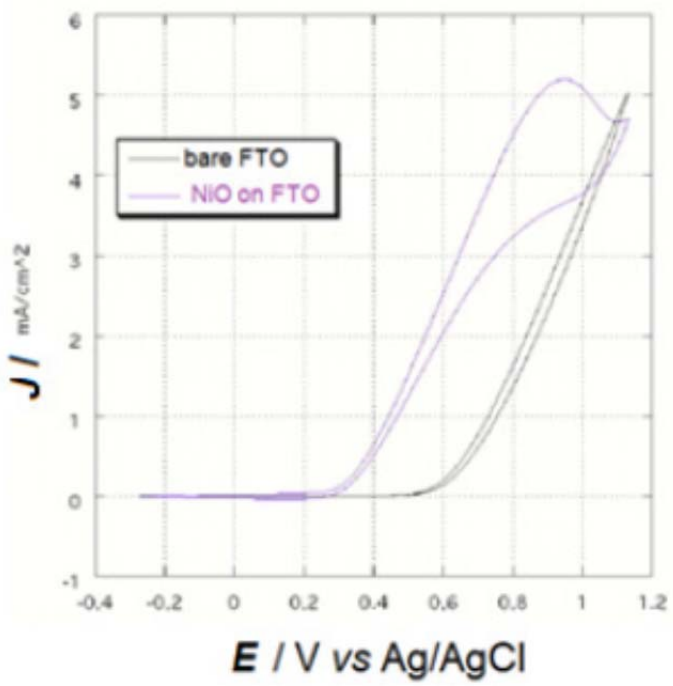

FIGURE 21. DARK VOLTAMMOGRAM OF NIO/FTO (VIOLET CURVE) AND UNCOATED FTO (BLACK CURVE) WITH I_3^-/I^- REDOX COUPLE. SCAN RATE: 20 MV/S. ELECTROLYTE COMPOSITION: 0.2 M I^-/0.02 M I_2 IN MPN. THE THREE-ELECTRODE CELL HAD COATED/UNCOATED FTO AS WORKING ELECTRODE, AG/AGCL AS REFERENCE ELECTRODE, AND PT AS COUNTER ELECTRODE. ADAPTED FROM REF. 56.

Another phenomenon limiting the FF in nanostructured NiO-based *p*-DSCs through the diminution of LHE parameter (Eq. 5) is the electrochromism of NiO. [58] This effect consists in the change of the optical absorption properties of NiO thin film induced by charge injection in the oxide film. Charge injection in NiO can be driven either electrochemically in dark conditions, [56] or photoinduced via dye-sensitizer mediation (see above). When holes are injected in NiO [this corresponds to the conversion of Ni (II) into Ni (III), no matter of the actual mechanism of injection] [59] the metal oxide gets more conductive electronically [60, 61] and at the same time undergoes a negative variation of its optical transmission with resulting darkening. [58] This is equivalent to say that Ni (III) represent colour centres for oxidized mesoporous NiO. A consequence of this effect is the decrease of the efficiency with which the sensitizer photoinjects holes in partially oxidized NiO. A decrease of the intrinsic

optical transmission of the metal oxide brings about a subtraction of the luminous energy available for the re-excitation of regenerated dye. Such a decrease of useful luminous energy will be mostly suffered by the dye-sensitizer anchored on the sub-layers of the film that are more distant from the source of excitation. In case of front illumination of the DSC, the most suffering sub-layer will be that portion of the oxide interfacing the electrolyte, whereas for back illumination the less illuminated sub-layer will result that portion of metal oxide at NiO/FTO interface. [56] The increase of oxide film thickness will also play a detrimental role on LHE because of the intrinsic optical absorption of NiO in the neutral state, as well. [19] As a consequence of that, thick films of mesoporous NiO, e.g. with thickness $l > 5$ micron, cannot be proficiently used as photocathodes in *p*-DSC if one intends to increase the short-circuit current density and the open circuit photo-potential of the PEC. A critical range of film thickness $2 < l < 4$ micron must be then taken into account when nanoporous NiO is the photocathode used in *p*-DSCs if the phenomenon of self-absorption has to be limited. [19] A (small) advantage correlated to the latter phenomenon is the possibility of photogenerating charge carriers in bare mesoporous NiO when it absorbs light in its broad characteristic range 300-500 nm (**Figures 22** and **23**). Some research groups have considered the chemical doping of NiO to alter and, possibly, diminish the phenomenon of NiO self-absorption in the near UV-visible range through the modification of the electronic structure of the oxide matrix while preserving the feature of nanoporosity (**Figure 24**). [62]

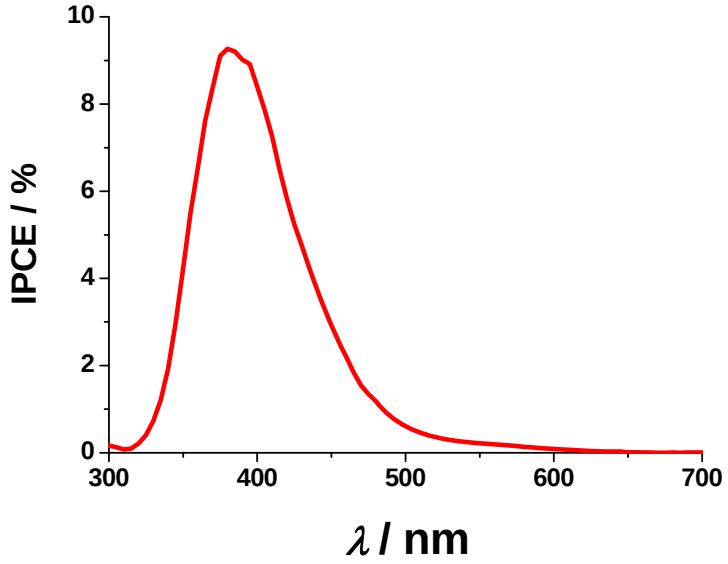

FIGURE 22. IPCE SPECTRUM OF THE *P*-DSC UTILIZING MESOPOROUS NIO IN THE BARE STATE AS PHOTOACTIVE CATHODE. REDOX MEDIATOR: I_3^-/I^- IN METHOXY-PROPIONITRILE. ADAPTED FROM REF. 56.

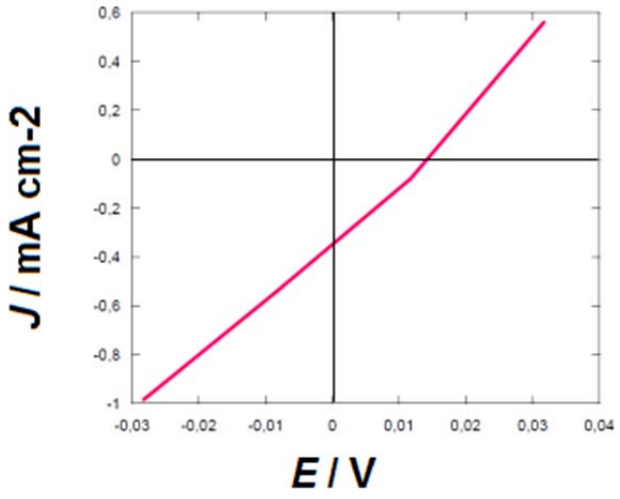

FIGURE 23. *JV* CURVE OF THE *P*-DSC UTILIZING UNSENSITIZED MESOPOROUS NIO AS PHOTOACTIVE CATHODE. V_{OC} = 11.7 MV; J_{SC} = -0.358 MA CM^{-2}; FF = 31.3 %; OVERALL EFFICIENCY = 0.000945 %. THIS EXPERIMENT SHOWS THAT BARE MESOPOROUS NIO IS PHOTOELECTROCHEMICALLY ACTIVE. ADAPTED FROM REF. 56.

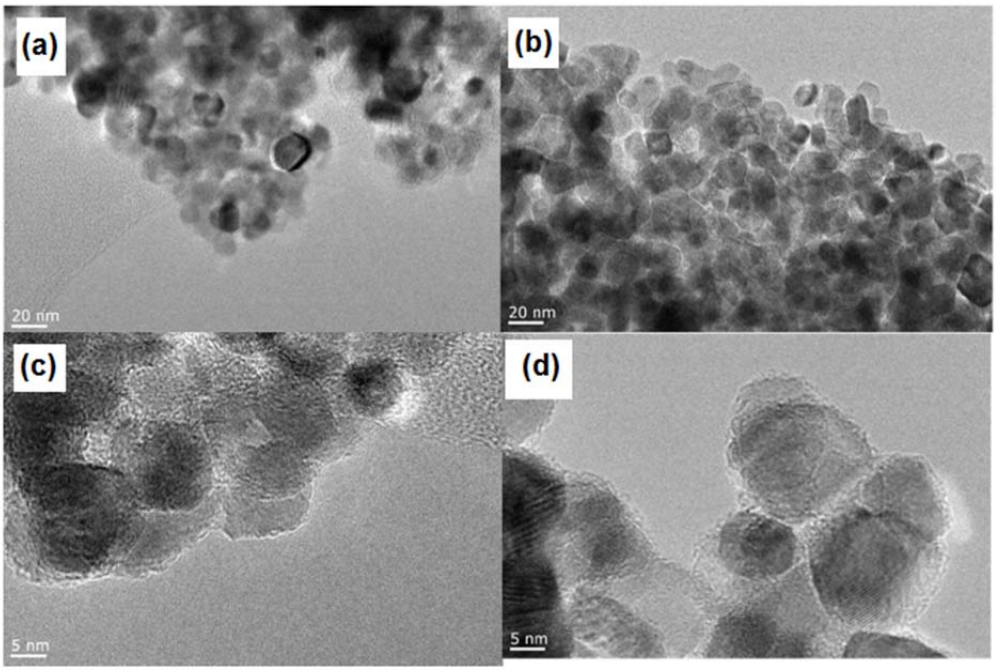

FIGURE 24. TEM IMAGES AT DIFFERENT MAGNIFICATIONS FOR (A,C) NANOPOROUS NIO AND (B,D) NANOPOROUS MG-DOPED NIO. ADAPTED FROM REF. 62.

The most common dopants were chosen among cations with little ionic radius, e.g. Li^+ [63-65] or Mg^{2+}, [62] which were introduced in the oxide at concentration levels of few percent with respect to Ni atoms. Changes of the optical absorption with dopant concentration were observed in passing from undoped to doped NiO (**Figure 25**), [63] but these not always corresponded to the desired bleaching of the mixed oxide.

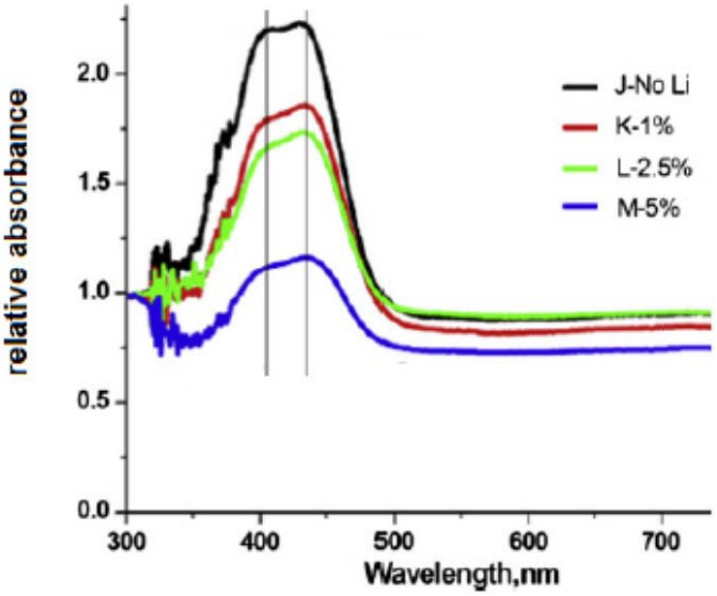

FIGURE 25. CHANGES OF RELATIVE ABSORBANCE IN NIO SAMPLES ($1.8 \leq L \leq 2.1$ micron) WITH VARIABLE LEVEL OF DOPANT CONCENTRATION. ADAPTED FROM REF. 63.

Beside self-absorption, other factors that could affect negatively the photoelectrochemical performance of NiO photocathodes in *p*-DSCs at the level of charge transport through the oxide itself are charge storage, [53, 66] internal recombination and charge trapping. [67] For the analysis of these phenomena, the relevant kinetic parameters to determine are τ_h, the hole transport time (τ_{tr}), the hole diffusion coefficient (D_h) and the hole diffusion length (L_D). [68] All these parameters are potential dependent and light-intensity dependent through the photo-potential and the photocurrent density (**Figures 26-29**). [50] D_h, L_D, τ_{tr}, and τ_h are correlated through the expressions: [68]

$$\tau_{tr} / \tau_h = (l / L_D)^2 \quad \{10a\}$$

$$L_D = (D_{h^+} \tau_{tr})^{0.5} \quad \{10b\}$$

The most abrupt changes of kinetic parameters with the potential E occur in the proximity of the open circuit potential value at which the transition from a regime of stationary charge distribution to a regime of mobile charge transport takes place when $E < V_{oc}$. The term of efficiency that is mostly affected by the kinetic parameters of Eqs. 10a and b is the efficiency of charge collection [$\eta_{coll}(\lambda)$], i.e. the fraction of the photoinjected charges at a given wavelength λ, which manages to reach the external circuit.

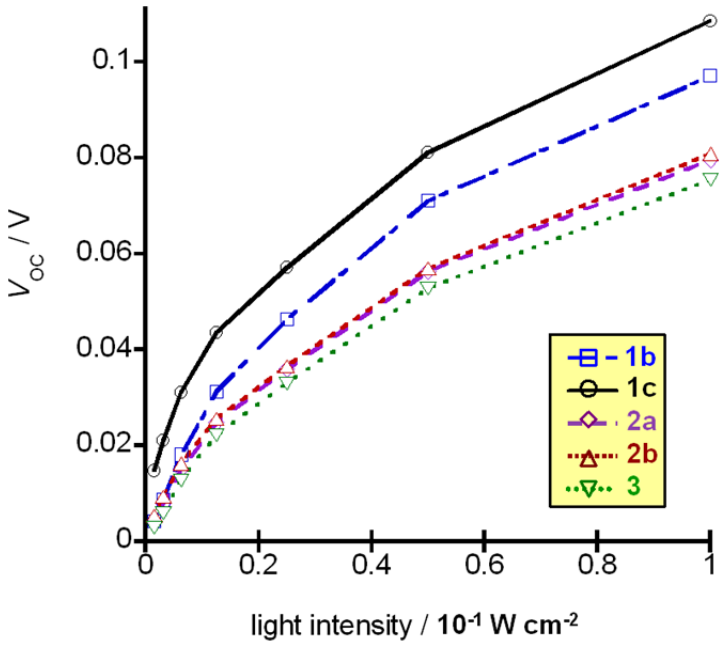

FIGURE 26. VARIATION OF THE OPEN CIRCUIT POTENTIAL (V_{OC}) WITH INCIDENT LIGHT INTENSITY FOR THE *p*-DSCs UTILIZING DIFFERENTLY DEPOSITED NiO PHOTOCATHODES. SENSITIZER: P1; REDOX SHUTTLE: I_3^-/I^-; SAMPLE AREA: 0.7 cm^2. THE CHARACTERISTICS OF SAMPLES 1-3 ARE REPORTED IN THE CAPTION OF TABLE 2 (*VIDE INFRA*). NIO FILMS HAVE THICKNESS VALUES IN THE RANGES: 1-2 μm (SAMPLES 1B AND 2A); 2-3 μm (SAMPLE 3); 3-4 μm (SAMPLE 2B); 5-6 μm (SAMPLE 1C).ADAPTED FROM REF. 19.

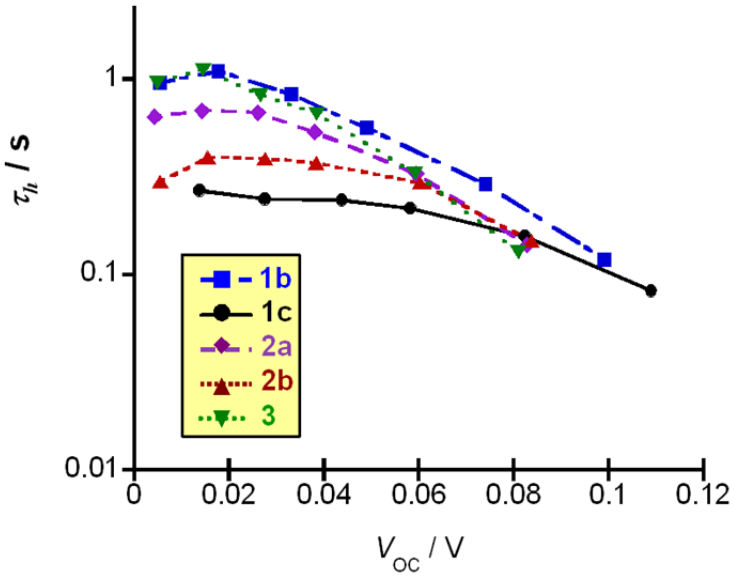

FIGURE 27. VARIATION OF CHARGE CARRIERS (HOLES) LIFETIME (τ_h) WITH THE V_{OC} VALUES DETERMINED AT DIFFERENT INCIDENT LIGHT INTENSITIES FOR THE *p*-DSCs UTILIZING DIFFERENT NiO PHOTOCATHODES. SENSITIZER: P1; REDOX SHUTTLE: I_3^-/I^-; SAMPLE AREA: 0.7 cm^2. THE CHARACTERISTICS OF MESOPOROUS NiO SAMPLES 1-3 ARE REPORTED IN THE CAPTION OF TABLE 2 (*vide infra*). INCIDENT LIGHT INTENSITY RANGES IN THE INTERVAL: 10^{-3}-10^{-1} W cm^{-2}. NiO FILMS HAVE THICKNESS VALUES IN THE RANGES: 1-2 μm (SAMPLES 1B AND 2A); 2-3 μm (SAMPLE 3); 3-4 μm (SAMPLE 2B); 5-6 μm (SAMPLE **1c**). ADAPTED FROM REF. 19.

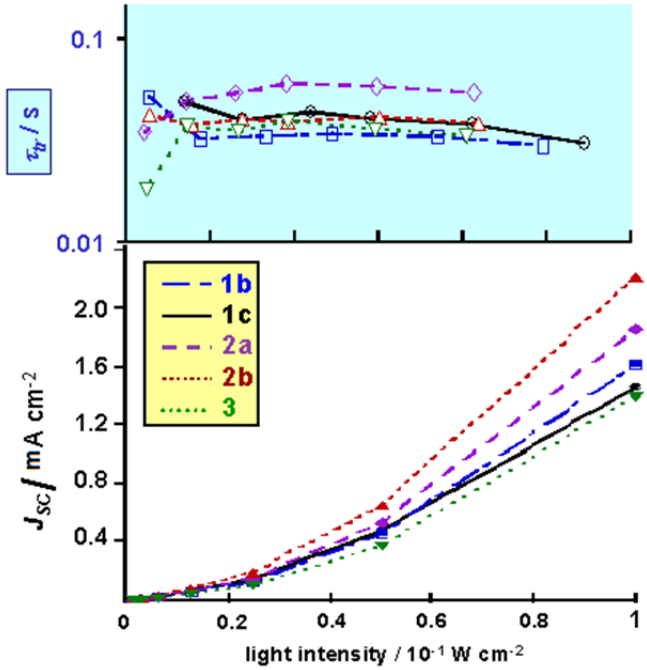

FIGURE 28. VARIATIONS OF THE HOLE TRANSPORT TIMES (τ_{tr}, OPEN SYMBOLS) AND THE CATHODIC SHORT CIRCUIT CURRENT DENSITY (J_{SC}, FULL SYMBOLS) VALUES DETERMINED AT DIFFERENT INCIDENT LIGHT INTENSITIES FOR THE *p*-DSCs UTILIZING DIFFERENT NIO PHOTOCATHODES. SENSITIZER: P1; REDOX SHUTTLE: I_3^-/I^-; SAMPLE AREA: 0.7 cm^2. THE CHARACTERISTICS OF MESOPOROUS NiO SAMPLES 1-3 ARE REPORTED IN THE CAPTION OF TABLE 2 (*vide infra*). NiO SAMPLES 1-3 DIFFER FOR THE THICKNESS: 1-2 μm (SAMPLES 1B AND 2A); 2-3 μm (SAMPLE 3); 3-4 μm (SAMPLE 2B); 5-6 μm (SAMPLE 1C). ADAPTED FROM REF. 19.

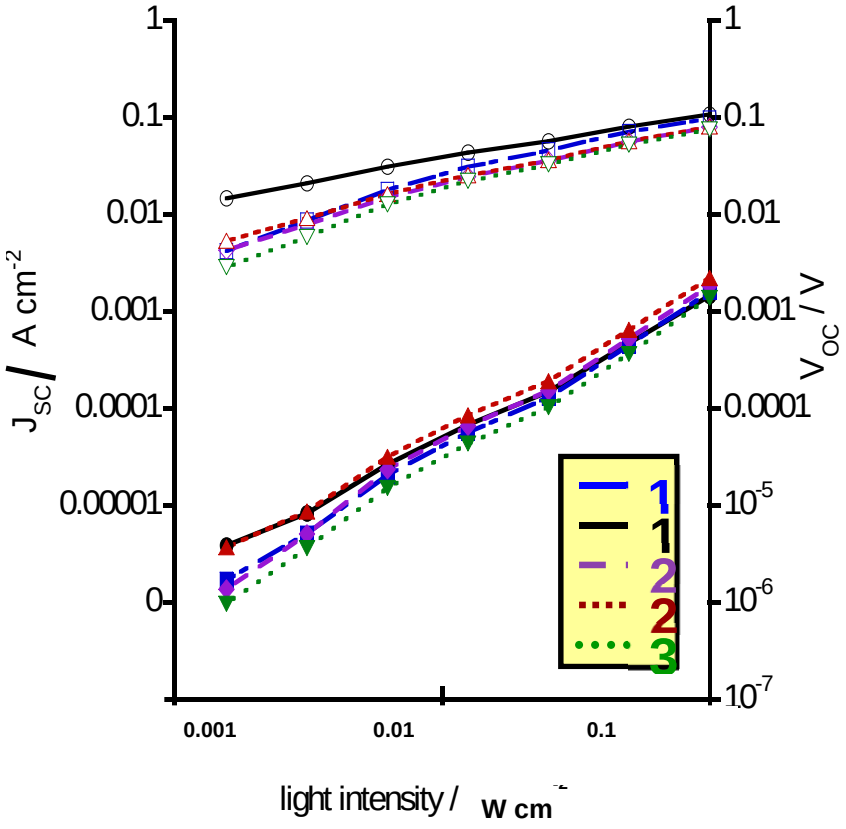

FIGURE 29. VARIATIONS OF V_{OC} (OPEN SYMBOLS) AND J_{SC} (FULL SYMBOLS) WITH THE LOGARITHM OF THE INCIDENT LIGHT INTENSITY FOR THE *p*-DSCs UTILIZING DIFFERENTLY DEPOSITED NiO PHOTOCATHODES. SENSITIZER: P1; REDOX SHUTTLE: I_3^-/I^-; SAMPLE AREA: 0.7 cm^2. THE CHARACTERISTICS OF MESOPOROUS NiO SAMPLES 1-3 ARE REPORTED IN THE CAPTION OF TABLE 2 (*VIDE INFRA*). NiO SAMPLES 1-3 DIFFER FOR THE THICKNESS: 1-2 μm (SAMPLES 1B AND 2a); 2-3μm (SAMPLE 3); 3-4 μm (SAMPLE 2b); 5-6μm (SAMPLE 1c). ADAPTED FROM REF. 19.

This efficiency term depends indirectly on the various kinetic factors according to the relationship: [69]

$$\eta_{coll}(\lambda) = \frac{\{-\alpha(\lambda)\cdot L_D\cdot\left[\cosh\left(l/L_D\right)\right]+\sinh\left(l/L_D\right)+\alpha(\lambda)\cdot L_D\cdot exp[-\alpha(\lambda)\cdot l]\}\cdot\alpha(\lambda)\cdot L_D}{[1-\alpha^2(\lambda)\cdot L_D{}^2]\cdot\{1-exp[-\alpha(\lambda)\cdot l]\ \}\cdot\cosh(l/L_D)} \quad \{11\}$$

in which $\alpha(\lambda)$ represents the absorption coefficient of the light-absorbing element (this can be either the dye-sensitizer or the semiconducting metal oxide itself) which photoinjects charge carriers in the metal oxide upon absorption of light with wavelength λ at a given light intensity I_{in}. In the determination of Eq.11, the assumption tacitly made is that light absorption occurs in a homogeneous way throughout the whole film. This is not necessarily the case for nanostructured mesoporous films of NiO that typically presents discontinuities in their morphology and compactness through their thickness (**Figures 30-32**). [19, 32] Moreover, homogeneity of the light absorption process will be prevented at those wavelengths that are strongly absorbed by any of the component (dye and NiO) of the sensitized electrode (case of high α, Eq.11). This is because charge photogeneration will occur almost exclusively on that portion of the film that is reached first by the radiation. This is particularly evident in those situations where huge differences are encountered between the *JV* and IPCE data obtained under front and back illumination. [56] Therefore, Eq.11, which is valid at the condition of homogeneous light absorption throughout the whole film thickness, will retain most of its validity also for nanostructured sensitized electrodes like the mesoporous NiO films here considered for *p*-DSCs (**Figures 30-32**), at the condition that light is weakly absorbed by the coloured electrode. [53]

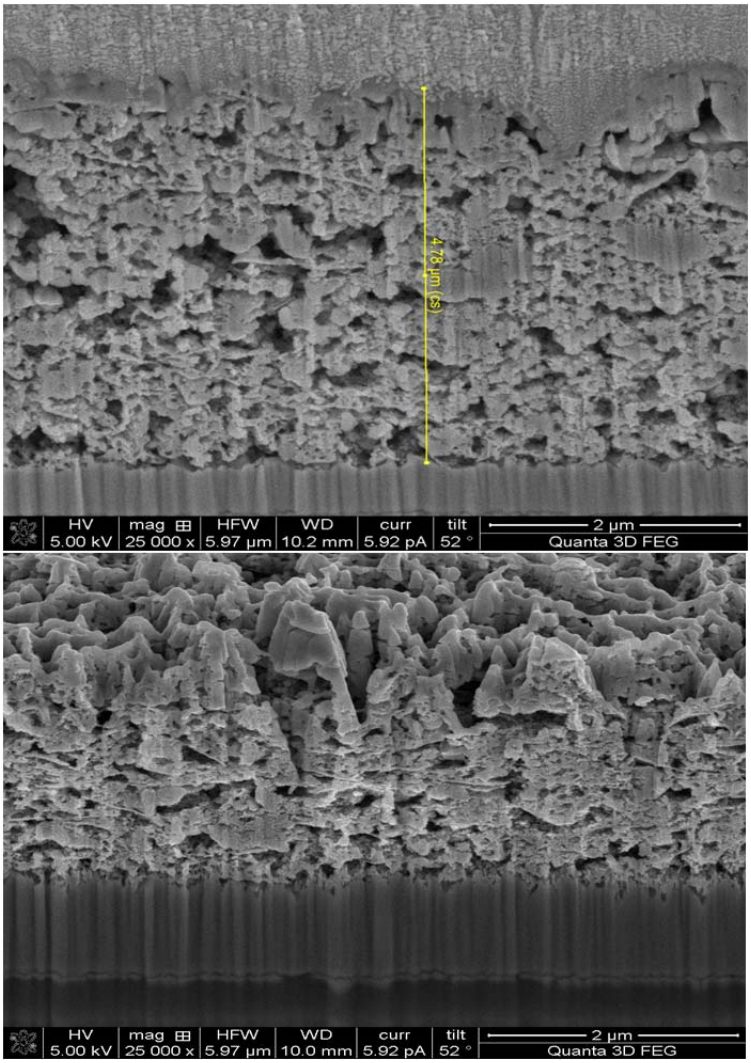

FIGURE 30. DUAL BEAM FIB–SEM IMAGE SHOWING THE CROSS SECTION OF TYPE 1 (TOP) AND TYPE 2 (BOTTOM) NIO COATINGS (SEE TABLES 1 AND 2 IN THE FOLLOWING FOR SAMPLE DESCRIPTION). FIB-SEM STANDS FOR FOCUSED ION BEAM–SCANNING ELECTRON MICROSCOPE. ADAPTED FROM REF. 19.

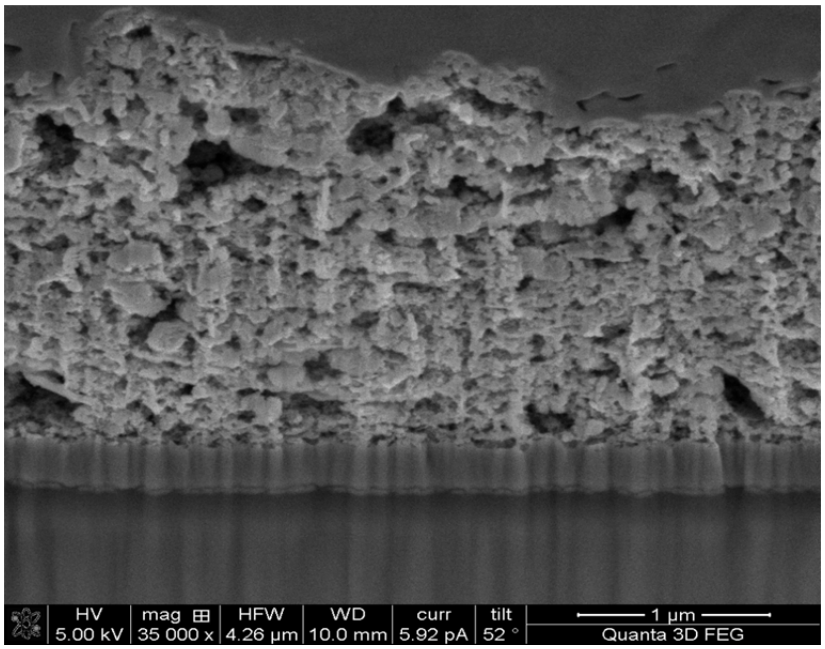

FIGURE 31. DUAL BEAM FIB–SEM IMAGE SHOWING THE CROSS SECTION OF TYPE 3 NIO LAYER (SEE TABLES 1 AND 2 FOR SAMPLE DESCRIPTION IN THE FOLLOWING). ADAPTED FROM REF. 32.

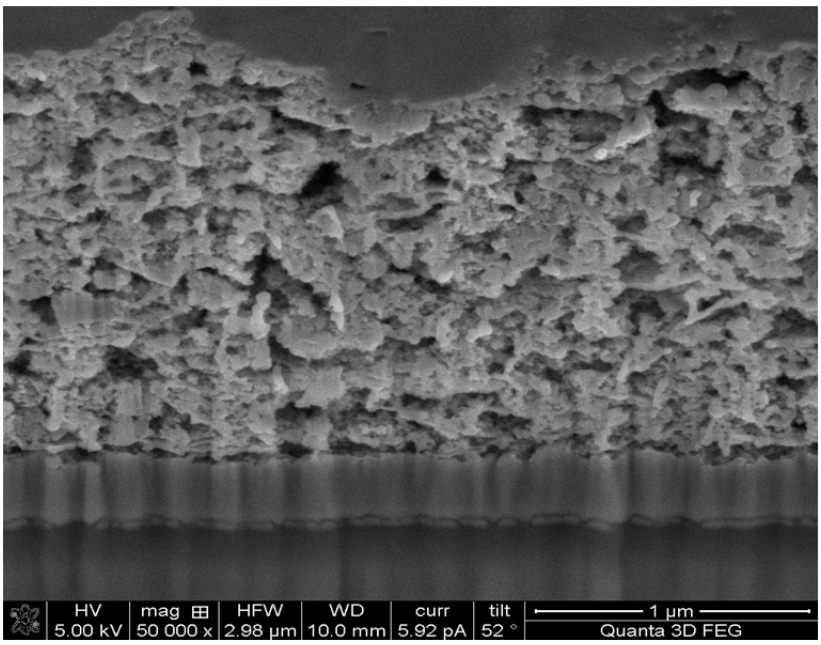

FIGURE 32. DUAL BEAM FIB–SEM IMAGE SHOWING THE CROSS SECTION OF TYPE 4 NIO COATING PREPARED THROUGH CONVENTIONAL SINTERING (SEE TABLES 1 AND 2 FOR SAMPLE DESCRIPTION IN THE FOLLOWING). ADAPTED FROM REF. 19.

Electrochemical Properties of Nanostructured Semiconductors

The charge storage properties of NiO are well established due to the extensive studies on the electrochemistry of NiO electrodes for various applications that range from energy storage to electrochromism or sensors, [70] beside photovoltaics. If the characteristic of charge storage of NiO represents an oxide property of great usefulness in some advanced technologies like electrochromic smart windows [71] or high-density energy batteries [72] are not so welcome when NiO is used in *p*-DSCs because of the severe limitations this phenomenon can impose on the transport of photoinjected charge carriers mainly through charge trapping. NiO in the configuration of thin film (either compact or mesoporous) undergoes both processes of solid-state electrochemical oxidation and reduction when polarized at opportune potential values. [73] The window of electrochemical stability of NiO is ample about 1.5 V and ranges between the extremes 1.7 and 3.2 V *vs* Li^+/Li (**Figure 33**). [73] Since NiO undergoes redox processes as a solid state material the accompanying exchange of ionic charge between NiO film and the electrolyte

must be taken necessarily into account in order to achieve electrical neutralization in the film. For the reduction process of NiO the overall reaction of charge compensation is: [74]

$$NiO + yM^{n+} + (ny)e^- \rightarrow M_yNiO \quad \{12\}$$

In Eq.12, M^{n+} represents a cation of opportune sizes that is inserted in the NiO structure according to a process of charge intercalation necessary to preserve electrical neutrality inside the metal oxide film. The reaction reported in Eq.12 is of poor practical interest when NiO electrochemistry is analyzed for DSC purposes since the uptake of electrons of in the CB of NiO is not occurring during the processes of charge photoinjection. For the electrochemical characterization of NiO with *p*-DSC finalities, the much more important one is the process of its electrochemical oxidation which consists in the dark electrochemical injection of holes in NiO from the electrical contact at the oxide/substrate interface. [18, 62] The oxidation of NiO conducted in this way would lead to an equivalent situation created in NiO when this is irradiated and holes photo-injection takes place at the oxide/electrolyte interface with the dye in the regenerated state. The regenerated state is the one reached by the dye after its interaction with the oxidized form of the redox mediator (**Figure 13**, see above).

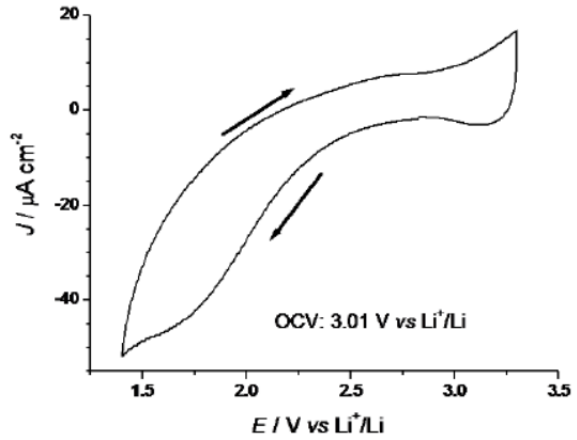

FIGURE 33. CYCLIC VOLTAMMETRY OF NIO COATINGS DEPOSITED VIA MICROBLASTING ON NI SUBSTRATE. NIOX FILM THICKNESS: 1.2 micron; ELECTROLYTE COMPOSITION: 0.5M LICLO4 IN PROPYLENE CARBONATE; SCAN RATE: 40 MV S-1. BLACK ARROWS INDICATE THE DIRECTION OF POTENTIAL SCAN. ADAPTED FROM REF. 73.

For the oxidation process of NiO the reactions of charge compensation will be: [18]

$$NiO + m\,X^{n-} \rightarrow Ni(II)_{1-mn}ONi(III)_{mn}(X)_m + (mn)\,e^- \quad \{13a\}$$

$$Ni(II)_{1-mn}ONi(III)_{mn}(X)_m + m\,X^{n-} \rightarrow Ni(II)_{1-mn}ONi(IV)_{mn}(X)_{2m} + (mn)\,e^- \quad \{13b\}$$

Reaction 13a, i.e. the first oxidation of NiO, will occur at lower potential values with respect to the second oxidation of NiO as reported in Eq. 13b. The features of NiO oxidation process depend on the nature of the electrolyte, i.e. if aqueous (**Figures 34** and **35**) [59, 75] or non-aqueous (**Figure 36**), [18, 76] and on the nature of the supporting electrolyte. [77] The analysis of the voltammograms conducted at different scan rates has evidenced that mesoporous NiO oxidation is a surface confined process as proved by the linear dependence of the better defined current peaks on the applied rate of potential scan in both aqueous (**Figure 37**) and non-aqueous (**Figure 38**)[76] electrolytic environments. The broad aspect of the various peaks of NiO oxidation and the corresponding reverse redox process (**Figures 34-36**) reflects the capacitive nature of NiO in the oxidized state, [75] i.e. in the state at the highest concentration of holes [or Ni(III) colour centres]. A distinctive feature of the solid state electrochemistry of nanostructured NiO is the clear recognition of the direct proportionality between the thickness of the mesoporous oxide and the amplitude of the current density peak (**Figure 39**). [59, 76] The correlation between film thickness and extent of exchanged current density in mesoporous nanostructured systems like the NiO here examined (**Figures 16, 18, 19, 30-32**) is due to the larger area of the surface of contact between electrode and electrolyte. Therefore, the more extended NiO/electrolyte interface of a thicker mesoporous electroactive film will result in much larger current densities with respect to a thinner electroactive film which undergoes equal electrochemical processes if the two samples possess the same geometrical area. Another phenomenon typical of nanostructured mesoporous NiO is the rapid dissolution of the oxide upon electrochemical oxidation in aqueous electrolyte. [59] This is experimentally evidenced by the observation of the decrease of current upon continuous

cycling of the mesoporous film within the potential range of NiO oxidation (**Figure 40**). Such an effect has been ascribed to the following mechanisms of charge compensation in oxidized NiO when its electroactivity is tested in aqueous electrolyte: [59]

$$NiO(OH)_{n+1}(H_2O)_{p-1} \rightarrow NiO(OH)_{n+2}(H_2O)_{p-2} + e^- + H^+ \quad \{14a\}$$

or

$$NiOO(OH)_{m-1} \rightarrow NiO_2(OH)_{m-2} + e^- + H^+ \quad \{14b\}$$

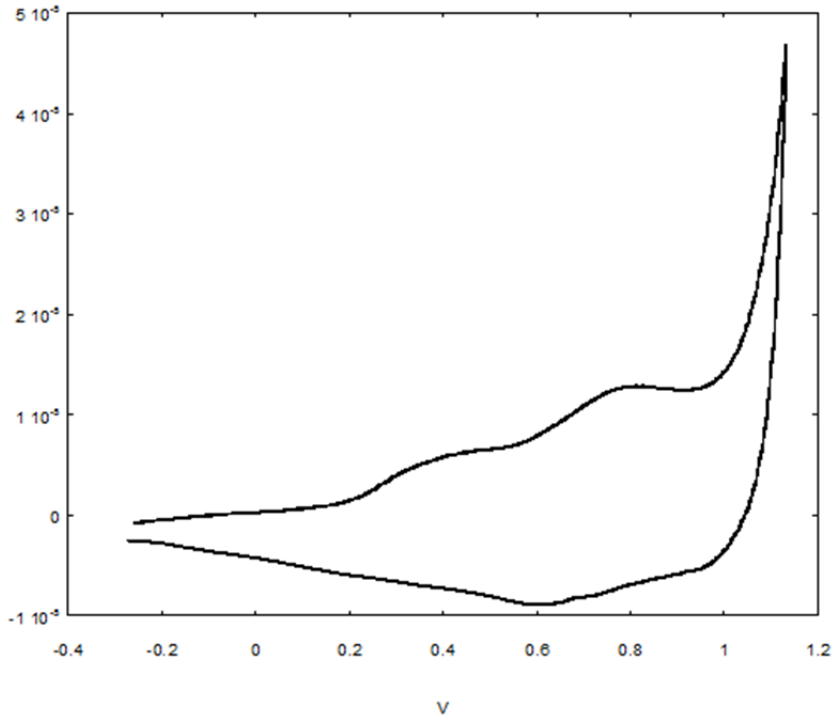

FIGURE 34. TYPICAL DOUBLE-PEAKED CYCLIC VOLTAMMETRY OF MESOPOROUS NIO IN A THREE-ELECTRODE CELL AT THE SCAN RATE OF 10 MV S^{-1}. ELECTROLYTE COMPOSITION: 0.2 M KCL, 0.01 M KH_2PO_4 AND 0.01 M NA_2HPO_4 IN WATER. CURRENT DENSITY (J) ON THE Y-AXIS IS EXPRESSED IN A CM^{-2}; POTENTIAL VALUES (V) ARE REFERRED TO THE POTENTIAL OF THE AG/AGCL REDOX COUPLE. ADAPTED FROM REF. 59.

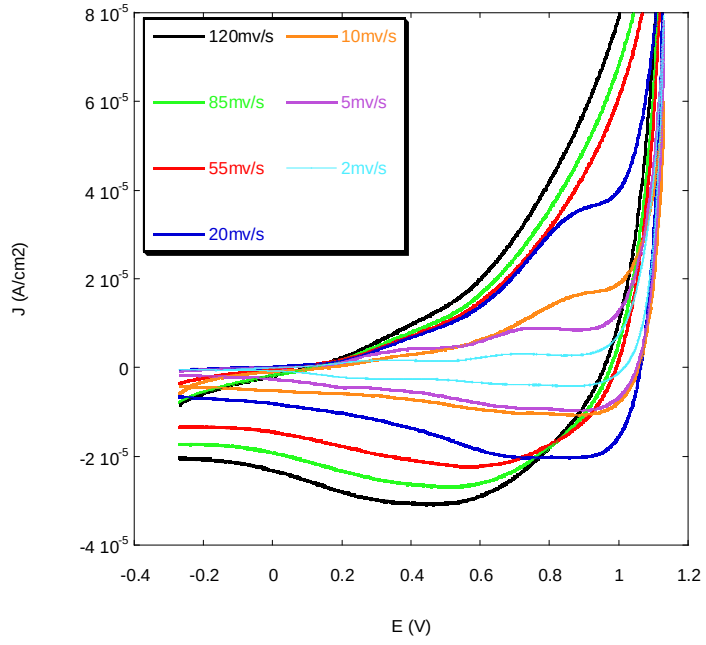

FIGURE 35. CYCLIC VOLTAMMETRIES OF NiO IN A THREE-ELECTRODE CELL AT DIFFERENT SCAN RATES IN DARK CONDITIONS. ELECTROLYTE COMPOSITION AND CELL CONFIGURATION SAME AS IN FIGURE 34. ADAPTED FROM REF. 59.

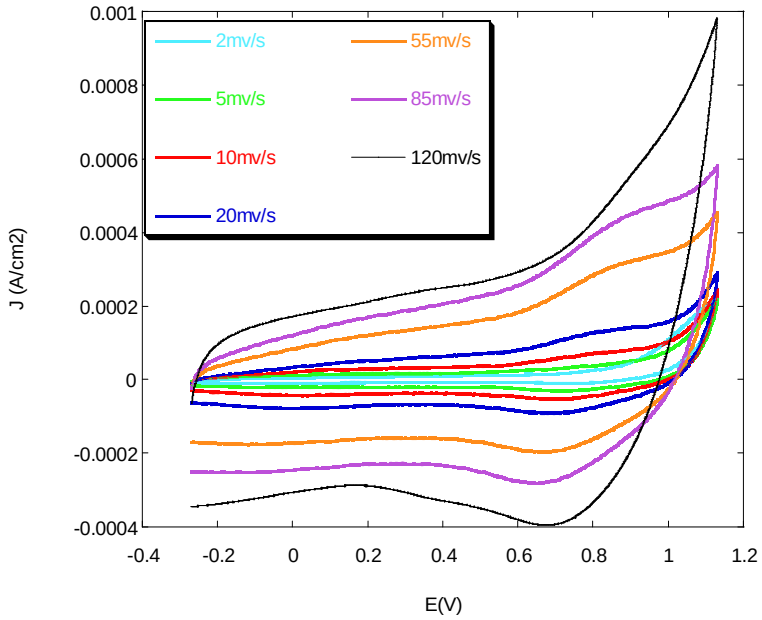

FIGURE 36. CYCLIC VOLTAMMETRIES OF MESOPOROUS NiO IN A THREE-ELECTRODE CELL AT DIFFERENT SCAN RATES. ELECTROLYTE COMPOSITION: 0.2 M N $(C_2H_5)_4ClO_4$ in MPN. POTENTIAL VALUES ARE REFERRED TO THE POTENTIAL OF Ag/AgCl REDOX COUPLE. ADAPTED FROM REF. 18.

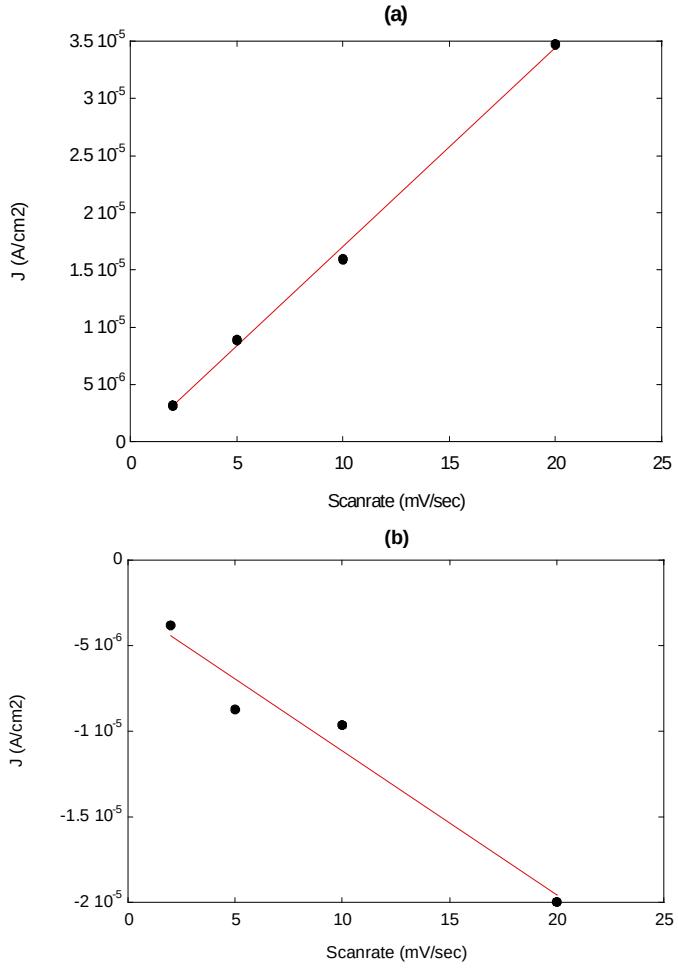

FIGURE 37. (a, TOP) LINEAR TREND OF THE FIRST ANODIC PEAK CORRESPONDING TO THE FIRST PROCESS OF NANOPOROUS NiO OXIDATION; (b, BOTTOM) LINEAR TREND OF THE BROAD CATHODIC PEAK CORRESPONDING TO THE NEUTRALIZATION OF OXIDIZED NiO. DATA EXTRAPOLATED FROM FIGURE 35. ADAPTED FROM REF. 59.

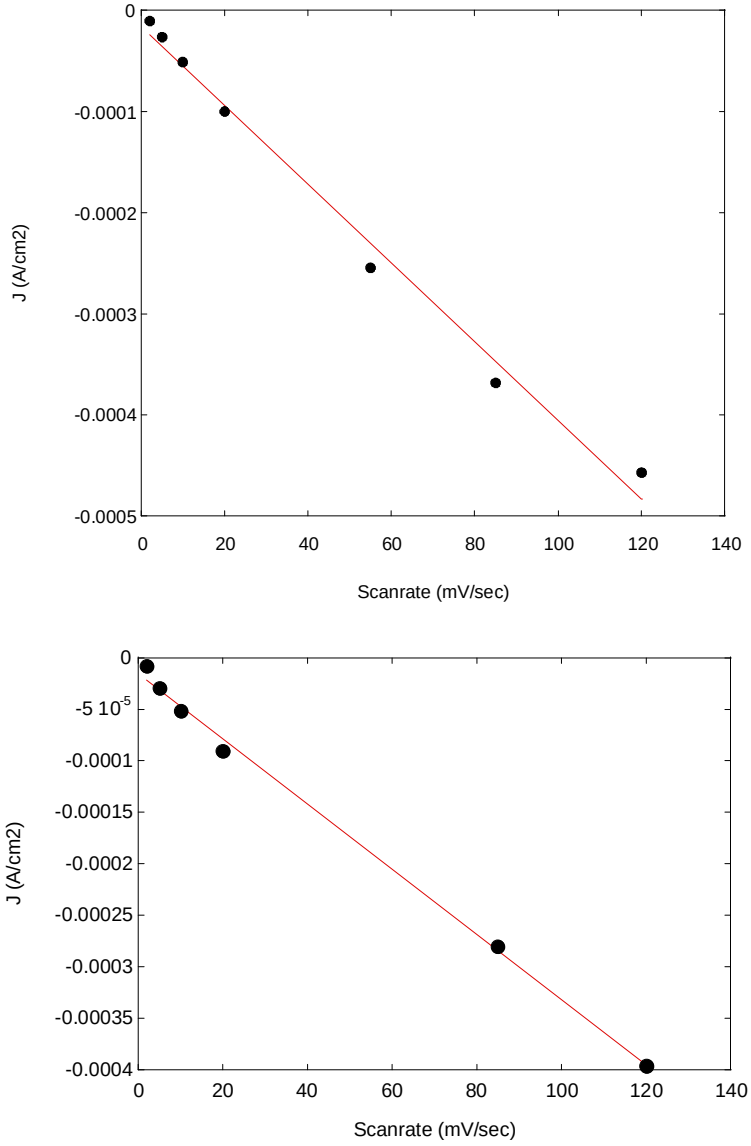

FIGURE 38. LINEAR VARIATION OF THE CATHODIC PEAK OBSERVED IN CORRESPONDENCE OF THE NEUTRALIZATION OF MESOPOROUS NiO AT AROUND 0.7 V *vs* Ag/AgCl UPON MODULATION OF THE SCAN RATE. DATA EXTRAPOLATED FROM VOLTAMMOGRAMS RECORDED IN (TOP) 0.2 M $LiClO_4$ in MPN, AND (BOTTOM) IN THE SAME ELECTROLYTE OF FIGURE 36. ADAPTED FROM REF. 76.

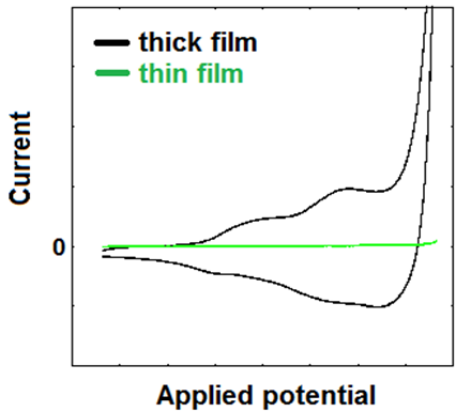

FIGURE 39. DEPENDENCE OF THE SHAPE OF THE CYCLIC VOLTAMMETRY SHAPE ON THE THICKNESS OF MESOPOROUS NiO FILM. THE DIFFERENCE IS ASCRIBED TO THE DIFFERENT AMOUNT OF ELECTROACTIVE MATERIAL, i.e. NiO ELECTRODE, IN CONTACT WITH THE ELECTROLYTE. ADAPTED FROM REF. 59.

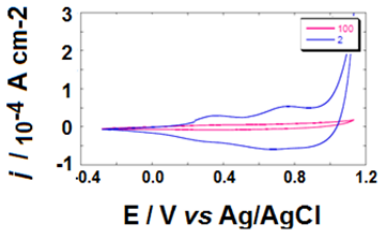

FIGURE 40. ELECTROCHEMICAL DISSOLUTION FOR MESOPOROUS NiO WHEN THE OXIDE IS CONTINUOUSLY CYCLED IN AQUEOUS ELECTROLYTE. THE NUMBERS IN THE LEGEND INDICATE THE CYCLE NUMBER. ADAPTED FROM REF. 59.

Such mechanisms of charge exchange between oxidized NiO with nanoporous morphology and ionic species from electrolytes has been reported to be a consequence of the hydration of NiO surface.[59,75] The latter process is activated on the surface sites of NiO that are associated to dangling bonds or to the uncompensated charges usually present on the electrode surface. The occurrence of a different mechanism of charge compensation in aqueous environment (Eqs. 14a and b) has been established by recording the voltammograms of the same NiO electrode in contact with alternating aqueous and non-aqueous electrolytes (**Figure 41**). [76]

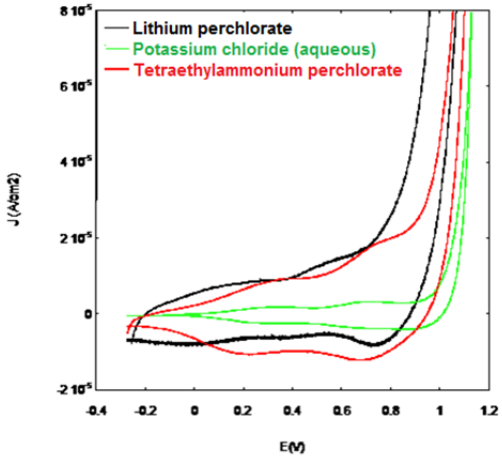

FIGURE 41. COMPARISON OF THE CYCLIC VOLTAMMETRIES OF MESOPOROUS NiO IN DIFFERENT ELECTROLYTES AT THE SCAN RATE OF 2 mV s^{-1}. ELECTROLYTE COMPOSITIONS: (BLACK TRACE) 0.2 M $LiClO_4$ in MPN; (GREEN TRACE) 0.2 M KCl IN WATER BUFFERED WITH DIHYDROGEN-/HYDROGEN-PHOSPHATE COUPLE; (RED TRACE) 0.2 M N $(C_2H_5)_4ClO_4$ in MPN. POTENTIAL VALUES ARE REFERRED TO THE POTENTIAL OF Ag/AgCl REDOX COUPLE. ADAPTED FROM REF. 76.

Such findings clearly indicate that there is no room for the employment of aqueous electrolytes in *p*-DSCs based on NiO photocathodes. An important consequence of the alteration of the oxidation state of the Ni centres in oxidized NiO is the modification of the charge transport properties and, consequently, of NiO electrical conductivity as verified with the technique of electrochemical impedance spectroscopy (EIS) when mesoporous NiO was polarized at different potential values (**Figures 42-44**). [42] Impedance spectra could distinguish in mesoporous NiO electrodes three main regimes characterized by different values of electrical conductivity. Such regimes reflected the existence of different extents of NiO oxidation as imposed by the application of system-specific potential values. [31] Such states of different electrical conductivity of NiO are dependent on the variations of the number of charge carriers the value of which is controlled by the applied electrical potential.

Moreover, it was clear that such conductivity changes in NiO depended also on the nature of the electrolyte that is involved in the charge compensation processes depicted in Eqs. 13a, 13b, 14a and 14b (see above). The EI spectra of bare mesoporous NiO in electrolytes that differ for the nature of solvent (H_2O or MPN) and supporting electrolyte, e.g. KCl, $LiClO_4$, $LiBF_4$ or $N(C_2H_5)_4ClO_4$, present the electrical response of the electrochemical system against a potential stimulus at varying frequency (typically in the range $10^{-3} \leq \nu \leq 10^5$ Hz). This technique offers then the opportunity of analyzing charge transport processes or charge redistribution processes having considerably different timescales. The processes of charge transport involved in the EI spectrum of mesoporous NiO when the range of applied frequencies is $10^{-3} \leq \nu \leq 10^5$ Hz are: i) the charge transfer process at the mesoporous NiO electrode/electrolyte interface; ii) the diffusion-controlled charge transport through the metal oxide skeleton. [74] The first process regards the ion compensation process occurring at the interface metal oxide/electrolyte upon

oxidation of NiO, whereas the second process (slower than the first one) is represented by the movement of the electronic charges introduced electrochemically through the oxide upon its oxidation. The latter process is typically diffusion-controlled in mesoporous semiconductors, [22] and might involve the tied displacement of charge compensating ions either intercalated in the structure (topotactic electrochemical reaction), or surface localized (electrochemical capacitor behaviour). A model of equivalent circuit that takes reasonably into account all these phenomena is the one proposed by Passerini *et al.*, [74] which is based on Randles circuit and is valid for NiO (either compact or mesoporous) when is polarized both anodically and cathodically (**Figure 45**). Upon polarization of mesoporous NiO in the range of its oxidation, i.e. in the potential regime leading to the electrochemical injection of holes, the resistive term R_{CT} (**Figure 45**) associated with the charge transfer resistance at the electrode/electrolyte interface is the term that undergoes the most significant changes and tends to decrease with potential increase (**Figures 42-44**). The corresponding variations span from few hundreds of Ohm at the highest potential of NiO polarization, to several thousands of Ohm for the lowest applied potential and when electrolytes manifest poor tendency of compensating the positive charge excess in oxidized NiO, e.g. case of $LiBF_4$ as supporting electrolyte. [77]

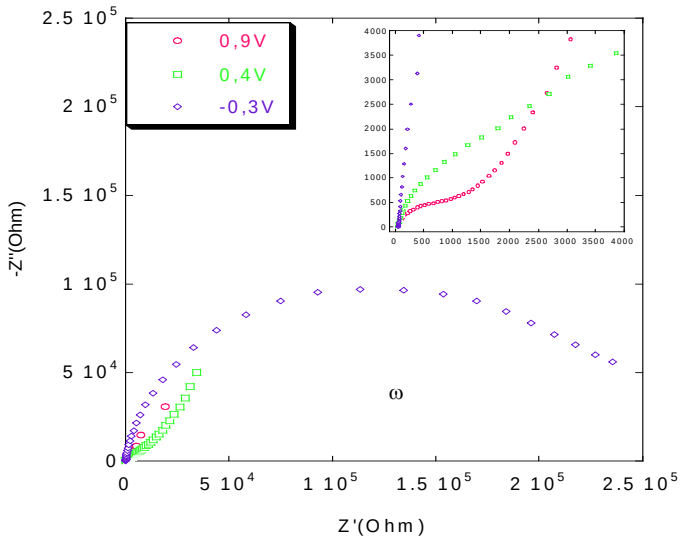

FIGURE 42. EIS OF MESOPOROUS NIO IN AQUEOUS ELECTROLYTE (COMPOSITION: 0.2 M KCl IN WATER BUFFERED WITH DIHYDROGEN-/HYDROGEN-PHOSPHATE COUPLE). THE NANOSTRUCTURED OXIDE WAS POLARIZED AT THREE DIFFERENT VALUES OF APPLIED POTENTIAL: (VIOLET DIAMONDS) -0.3 V *vs* Ag/AgCl; (GREEN SQUARES) + 0.4 V *vs* Ag/AgCl; (RED CIRCLES) + 0.9 V *vs* Ag/AgCl. THE INSET PRESENTS A ZOOM OF THE EI SPECTRUM IN THE HIGH FREQUENCY REGION. ADAPTED FROM REF. 42.

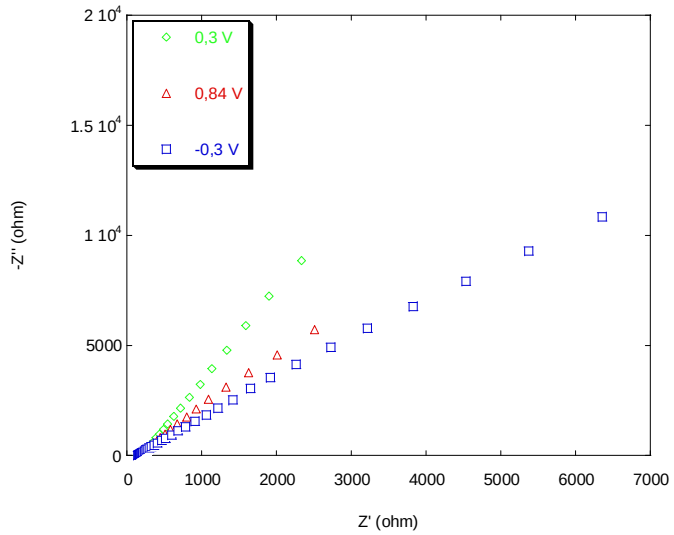

FIGURE 43. EI SPECTRA OF MESOPOROUS NiO IN NON-AQUEOUS ELECTROLYTE (COMPOSITION: 0.2 M $LiClO_4$ in MPN). THE NANOSTRUCTURED OXIDE WAS POLARIZED AT THREE DIFFERENT VALUES OF APPLIED POTENTIAL: (BLUE SQUARES) - 0.3 V *vs* Ag/AgCl; (GREEN DIAMONDS) + 0.4 V *vs* Ag/AgCl; (RED TRIANGLES) + 0.84 V *vs* Ag/AgCl. ADAPTED FROM REF. 42.

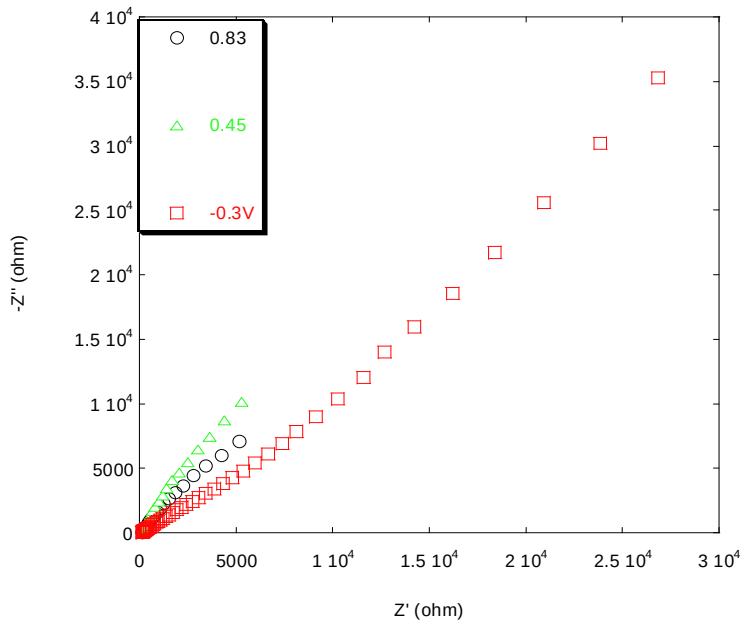

FIGURE 44. EI SPECTRA OF MESOPOROUS NiO IN NON-AQUEOUS ELECTROLYTE [COMPOSITION: 0.2 M $N(C_2H_5)_4ClO_4$ in MPN]. THE NANOSTRUCTURED OXIDE WAS POLARIZED AT THREE DIFFERENT VALUES OF APPLIED POTENTIAL: (RED SQUARES) - 0.3 V *vs* Ag/AgCl; (GREEN DIAMONDS) + 0.45 V *vs* Ag/AgCl; (BLACK CIRCLES) + 0.83 V *vs* Ag/AgCl. ADAPTED FROM REF. 42.

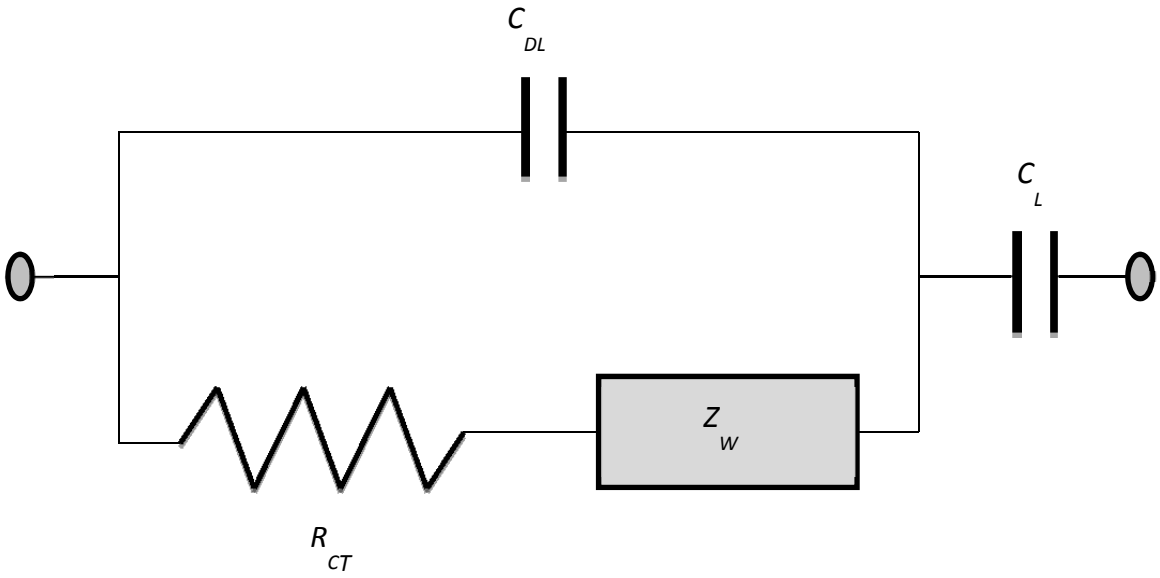

FIGURE 45. EQUIVALENT CIRCUIT FOR NIO ELECTRODES OXIDIZED AT DIFFERENT EXTENTS. C_{DL} = CAPACITANCE OF THE DOUBLE LAYER AT NIO ELECTRODE/ELECTROLYTE INTERFACE; R_{CT} = CHARGE TRANSFER RESISTANCE THROUGH NIO ELECTRODE/ELECTROLYTE INTERFACE; Z_W = WARBURG IMPEDANCE ASSOCIATED WITH CHARGE TRANSPORT THROUGH NIO_X ELECTRODE; C_L = LIMITING CAPACITANCE FOR NIO FILMS WITH FINITE THICKNESS. ADAPTED FROM REF.74.

Another important characteristic of the electrochemistry of nanostructured NiO for *p*-DSCs applications is the relatively scarce sensitivity of the process of NiO oxidation to the eventual presence of an anchored dye-sensitizer. [19,32,42] It has been generally observed that the only effect played by the colorant is the passivation of the NiO surface towards its oxidation in case the colorant does not undergo a process of oxidation in the potential range of anodic electroactivity for NiO (**Figures 46, 47**). [19,42] Effects of dye-induced passivation of NiO surface could be evidenced when differently deposited samples of mesoporous NiO (**Figures 30-32**) were sensitized with erythrosine B, P1, N719 and black dye, [56] whereas squaraines get oxidized in the same potential range of NiO oxidation and successively detach. [56]

The latter finding poses severe limitations on the use of squaraines as dye-sensitizers of cathodic DSCs based on mesoporous NiO photoactive electrodes. In fact, squaraine desorption can be prevented only in case of a very fast

process of dye regeneration and fast hole transport inside the oxide with respect to the detrimental process of electron back-donation from neutral/anionic sensitizer to oxidized NiO (reverse of processes a/b in **Figure 13**). [26]

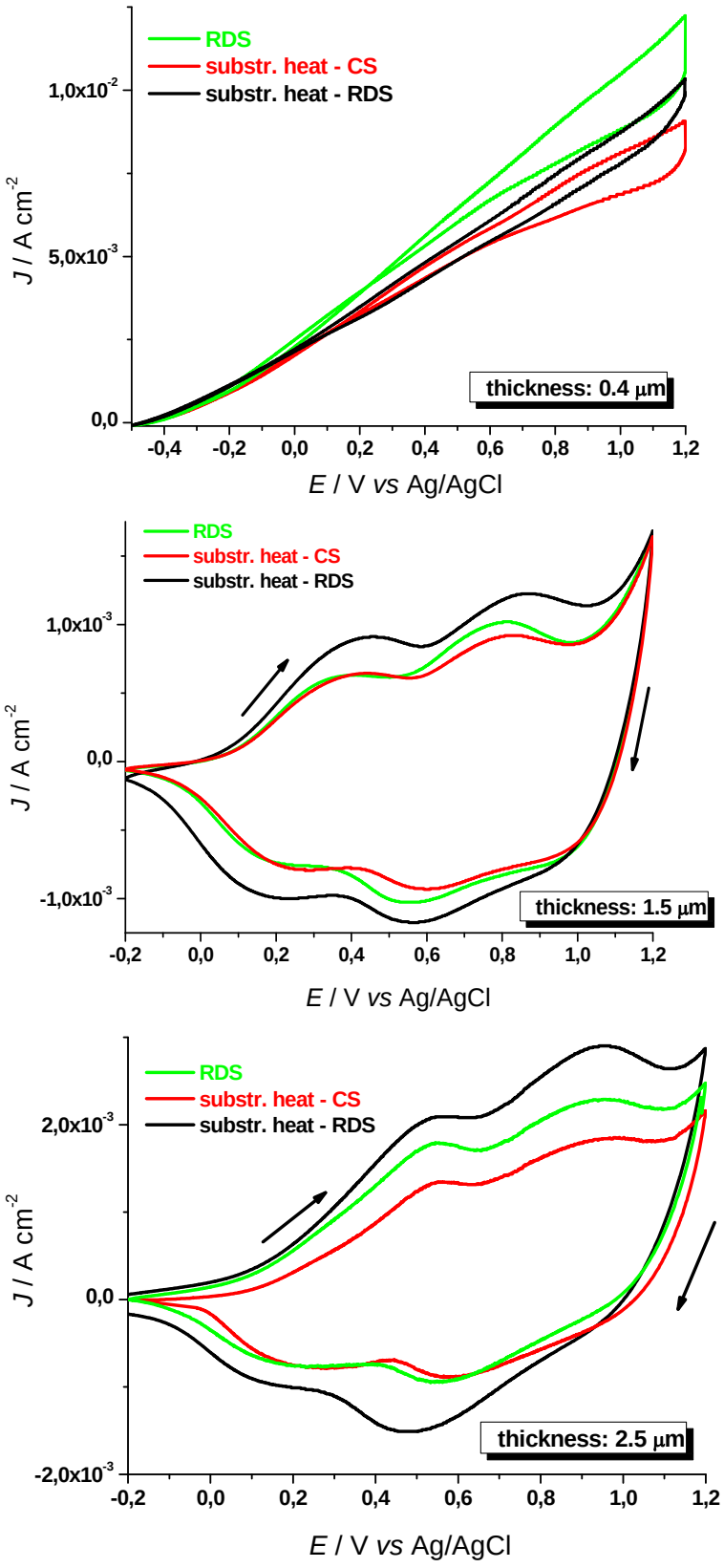

FIGURE 46. CYCLIC VOLTAMMETRIES OF DIFFERENTLY DEPOSITED NiO SAMPLES IN THE BARE STATE. CS: CONVENTIONAL SINTERING; RDS: RAPID DISCHARGE SINTERING. TOP: THINNER NiO SAMPLES; CENTRE: NiO SAMPLES WITH MEDIUM THICKNESS; BOTTOM: THICKER NiO SAMPLES. SCAN RATE: 40 mV s^{-1}; ELECTROLYTE COMPOSITION: 0.2 M KCl, 0.01 M KH_2PO_4 AND 0.01 M Na_2HPO_4 IN WATER. ARROWS INDICATE THE VERSE OF POTENTIAL SCAN. ADAPTED FROM REFS. 19 AND 42.

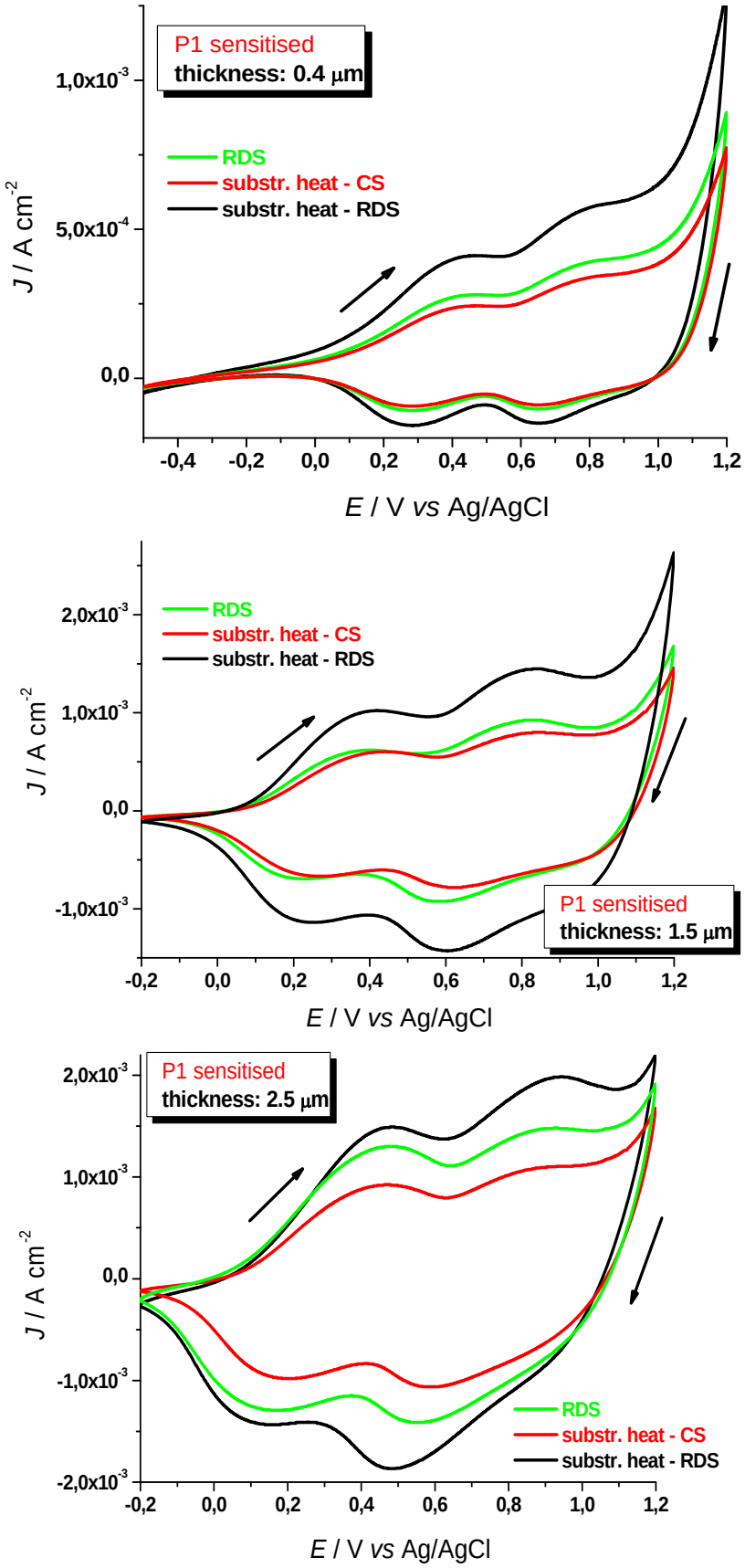

FIGURE 47. CYCLIC VOLTAMMETRIES OF DIFFERENTLY DEPOSITED NiO SAMPLES IN THE SENSITIZED STATE (DYE-SENSITIZER: P1). CS: CONVENTIONAL SINTERING; RDS: RAPID DISCHARGE SINTERING. TOP: THINNER NiO SAMPLES; CENTRE: NiO SAMPLES WITH MEDIUM THICKNESS; BOTTOM: THICKER NiO SAMPLES. SCAN RATE: 40 mV s^{-1}; ELECTROLYTE COMPOSITION: 0.2 M KCl, 0.01 M KH_2PO_4 AND 0.01 M Na_2HPO_4 IN WATER. ARROWS INDICATE THE VERSE OF POTENTIAL SCAN. ADAPTED FROM REF. 19.

Analysis of p-DSCs

Insofar the best photoelectrochemical performance of a *p*-DSC based on mesoporous NiO cathodes has been reported by Powar *et al*. [51] who affirmed that the overall efficiency of the *p*-type device was in the range 1.31-1.67 % when the NiO film was 2.5 micron thick (irradiated area: 0.16 cm^2), the electrolyte contained the couple Co(III)/Co(II) as redox mediator and lithium bis(trifluoromethanesulfonylimide) as supporting electrolyte, and the dye-sensitizer was PMI-6T-TPA (**Figure 8**). Under these experimental conditions, the corresponding IPCE of the record efficiency *p*-DSC presented a region of maxima slightly higher than 60 % in the broad spectral range 390-530 nm. Such an outstanding result has been the product of an evolution in the procedures of synthesis and the techniques of deposition of nanostructured NiO, as well as the consequence of the progress achieved in the design and realization of increasingly efficient dye-sensitizers (mostly of organic nature). Last but not least, an important contribution to the progress in *p*-DSCs came also from the definition of more opportune redox mediators with the couple Co(III)/Co(II) that is going to undermine the predominance of the so far more well-established couple I_3^-/I^-. The evolution of *p*-DSCs dyes structures for mesoporous NiO sensitization has occurred in several steps starting historically from erythrosine B (the benchmark) [16,33,78,79] and moving towards the so far unsurpassed PMI-6T-TPA [51-53] (by far the most advanced dye for highly performing cells with NiO). Intermediate increasing performances have been obtained with fast green, [42, 80] coumarines, [81] indigo dyes, [36 and references therein] P1, [19,41,55] GS1 and CAD3 sensitizers (**Figure 8**), [34,35] not to mention squaraines that are going to represent a new special (but also delicate) class of organic colorants (Chart 1) for NiO with a quite rapidly ascending trend (**Figure 15**, see above, and **Figure 48**). [26] In Table 3, the comparison of some excellent performing *p*-DSCs that differ for the preparation of the cathodic material, and for the nature of the dye-sensitizer is presented when the couple I_3^-/I^- consitutes the redox mediator. [28, 52, 55, 82-86]

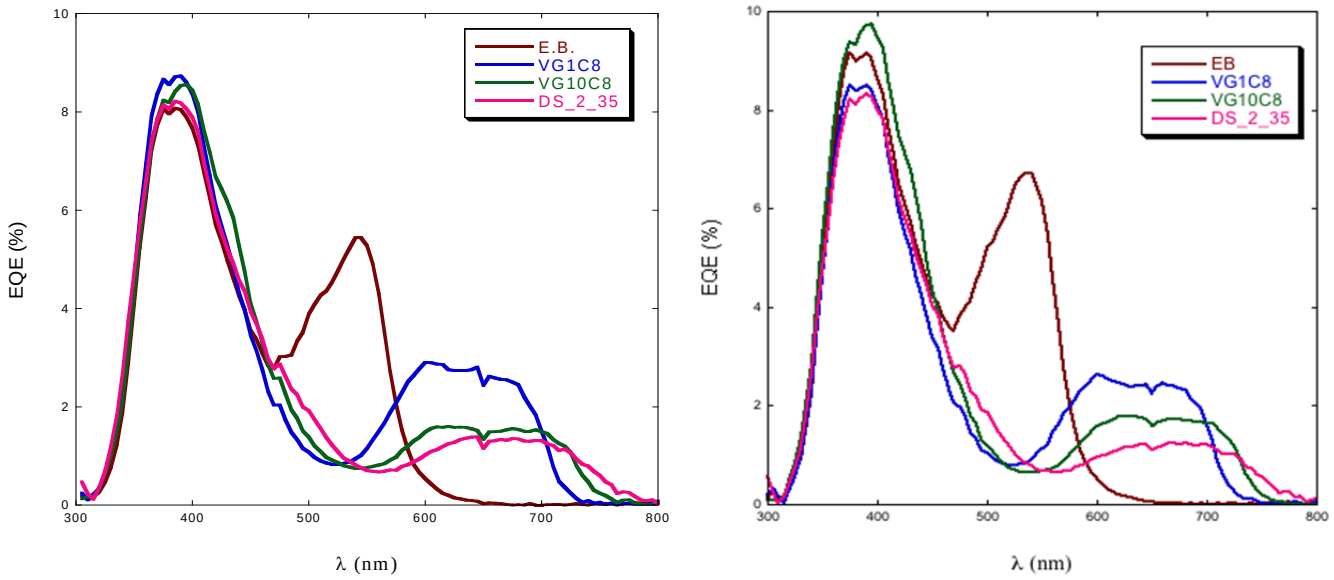

FIGURE 48. IPCE SPECTRA OF (LEFT) DYE-SENSITIZED SCREEN-PRINTED NiO AND (RIGHT) ALKALI TREATED SCREEN-PRINTED NiO PRIOR DYE-SENSITIZATION. EQE = EXTERNAL QUANTUM EFFICIENCY; EB = ERYTHROSINE B. FOR THE EXPLANATION OF THE SYMBOLS VG1C8, VG10C8 AND DS_2_35 SEE CHART 1 (*vide infra*). ADAPTED FROM REF. 26.

CHART 1. CHEMICAL STRUCTURES OF THE SQUARAINES FOR MESOPOROUS NIO SENSITIZATION

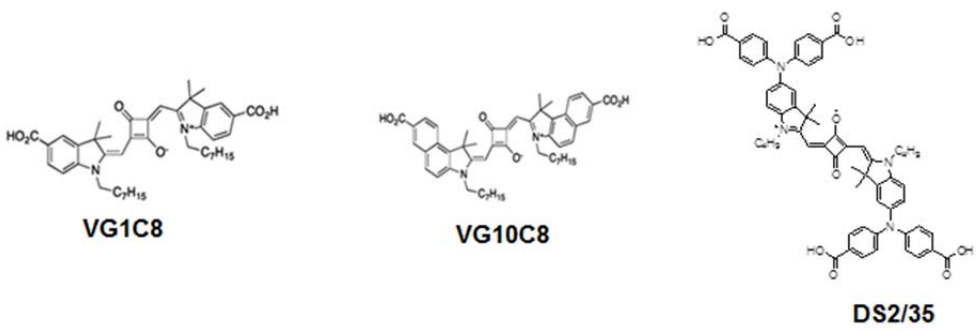

TABLE 1. COMPARATIVE LIST OF THE PARAMETERS DERIVED FROM THE *JV* CHARACTERISTIC CURVES OF THE *p*-DSCS ASSEMBLED WITH DIFFERENTLY PREPARED NIO PHOTOCATHODES AND DIFFERENT DYES. REDOX SHUTTLE: I_3^-/I^- IN ACETONITRILE.

Cathodic material	Sensitizer	l / micron	*overall efficiency* / %	V_{oc} / V	- J_{sc} / mA cm^{-2}	FF
NiO-sol gel (one step)[55]	**P1**	**1**	**0.120**	**0.106**	**3.01**	**0.370**
NiO-sol gel (two steps) [55]	**P1**	**0.8**	**0.150**	**0.084**	**5.48**	**0.340**
NiO-sol gel[82]	**PMI-NDI**	**2**	**0.073**	**0.120**	**1.76**	**0.345**
NiO-sol gel[83]	**DPP-NDI**	**---**	**0.090**	**0.155**	**1.38**	**0.400**
NiO-hydrothermal[86]	**C343**	**3.5**	**0.036**	**0.117**	**0.88**	**0.280**
NiO microballs[52]	**PMI-6T-TPA**	**2.8**	**0.380**	**0.214**	**5.15**	**0.34**
NiO microballs[52]	**PMI-6T-TPA**	**4.2**	**0.460**	**0.208**	**6.36**	**0.34**
NiO microballs[52]	**PMI-6T-TPA**	**6.0**	**0.430**	**0.185**	**7.0**	**0.33**
NiO np[28]	**PMI-2T-TPA**	**3.3**	**0.090**	**0.153**	**2.06**	**0.29**
NiO np[28]	**PMI-4T-TPA**	**3.3**	**0.190**	**0.176**	**3.40**	**0.32**
NiO np[28]	**PMI-6T-TPA**	**3.3**	**0.410**	**0.218**	**5.35**	**0.35**
NiO nanorods[85]	**PMI-6T-TPA**	**0.9**	**0.330**	**0.301**	**2.60**	**0.42**
NiO nanorods[85]	**PMI-6T-TPA**	**1.7**	**0.400**	**0.292**	**3.30**	**0.41**
NiO np on compact NiO[84]	**PMI-6T-TPA**	**0.8-1.0**	**0.140**	**0.350**	**1.32**	--

As thoroughly discussed in the critical paper of Daeneke *et al*., [53] even the best performing *p*-DSCs with NiO photoactive cathodes (Table 1) suffer constantly of relatively low fill factors that never exceed 0.45. Therefore, the most important achievements in the development of NiO based *p*-DSCs will have to focus on the increase of the fill factor with the first immediate target of FF ≥ 0.50. The first dye benchmark for testing mesoporous NiO as cathodic material of a *p*-DSC has been erythrosine b. [16] Because of that, for historical reasons the evolution of the quality of mesoporous NiO photoactive electrodes for *p*-DSC has been then tested utilizing this colorant as reference.[32, 33, 42, 76, 78, 79] The absorption spectrum of erythrosine b in solution presents a maximum at about 535 nm, which tends to broaden when this dye is anchored on nanostructured NiO (**Figure 49**). [33] Erythrosine sensitized NiO has a light red/purple appearance (**Figure 50**), which proves the phenomenon of electrode sensitization in the portion 450-590 nm of the visible range. The *JV* curves of the *p*-DSCs having differently deposited NiO electrodes sensitized with erythrosine b are shown in **Figures 51** and **52** with the corresponding relevant parameters listed in **Table 2**. The highest efficiencies obtained with erythrosine b as colorant of a *p*-DSC based on nanostructured NiO are just below 0.05 % with IPCE reaching at most 11 % in correspondence of the wavelength of maximum absorption (**Figure 53** and **Table 2**). Fill factors of erythrosine sensitized *p*-DSCs do not exceed 0.4 and fall commonly in the range 0.32-0.40.

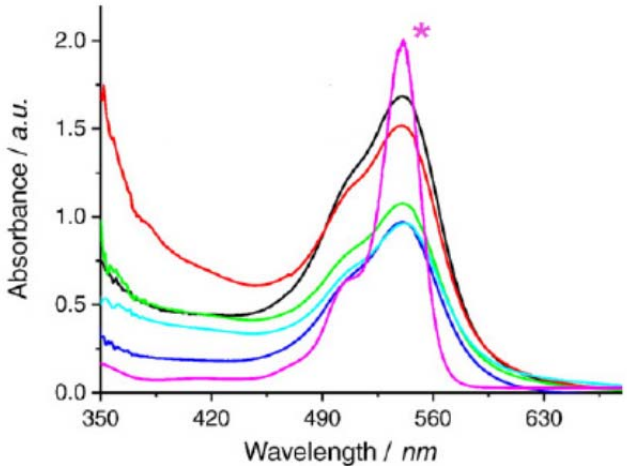

FIGURE 49. OPTICAL ABSORPTION SPECTRA OF ERYTHROSINE B IN SOLUTION (PROFILE INDICATED WITH THE ASTERISK *), AND IN THE ANCHORED STATE WHEN MESOPOROUS NIO IS THE SUBSTRATE (NIO THICKNESS: 1μm). THE SPECTRA OF ERYTHROSINE b ANCHORED ON NIO REFER TO SENSITIZED MESOPOROUS NIO SAMPLES PREPARED UNDER DIFFERENT CONDITIONS OF SINTERING. ADAPTED FROM REF. 33.

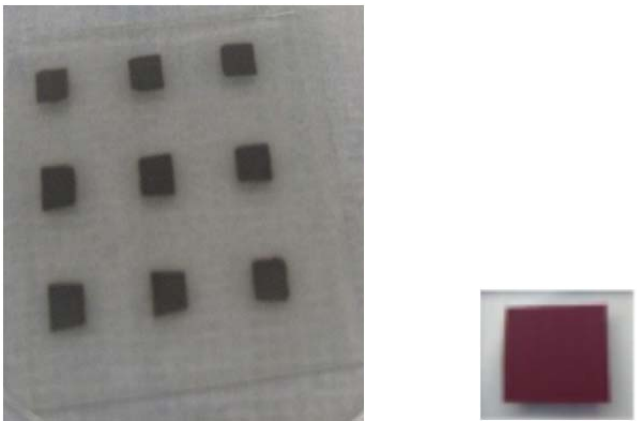

FIGURE 50. (LEFT) SET OF NiO THIN FILM ELECTRODES PREPARED VIA RAPID DISCHARGE SINTERING (RDS); (RIGHT) RDS NiO FILM TINCTURED WITH ERYTHROSINE B. FILM THICKNESS RANGE: 3-6 μm; ELECTRODE AREA: 0.25 cm². ADAPTED FROM REF. 33.

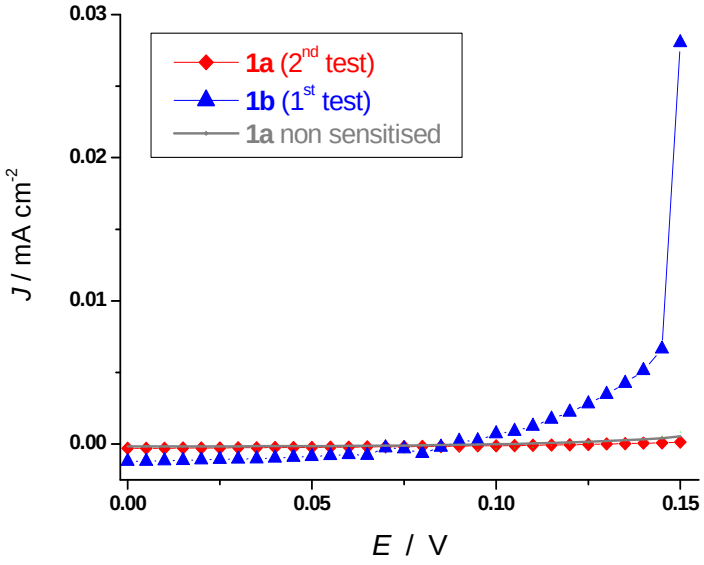

FIGURE 51. *JV* CURVES OF THE *p*-DSCs WITH NiO PHOTOCATHODES OF TYPE **1** DIFFERING FOR THE THICKNESS (a: 0.6 μm; b: 1-2 μm), WHICH HAVE BEEN SENSITIZED WITH ERYTHROSINE b. SAMPLE DESCRIPTION AND PARAMETERS HAVE BEEN REPORTED IN TABLE 2 (*vide infra*). ADAPTED FROM REF. 32.

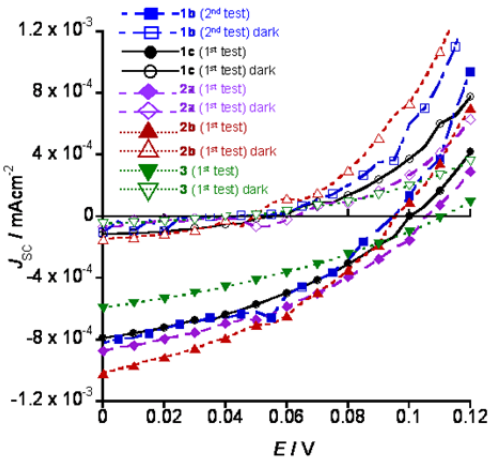

FIGURE 52. *JV* CURVES OF THE *p*-DSCS UTILIZING NiO PHOTOCATHODES OF DIFFERENT TYPES (1-3). NiO FILM THICKNESS VALUES ARE: 1-2 μm (SAMPLES 1B AND 2A); 2-3 μm (SAMPLE 3); 3-4 μm (SAMPLE 2B); 5-6 μm(SAMPLE 1C). REDOX SHUTTLE: I_3^-/I^- ; ACTIVE AREA OF THE DEVICE: 0.5-0.7 cm²; SENSITIZER: ERYTHROSINE b. SAMPLE DESCRIPTION AND PARAMETERS HAVE BEEN REPORTED IN TABLE 2 (*vide infra*). ADAPTED FROM REF. 32.

TABLE 2. LIST OF PARAMETERS OBTAINED FROM THE *JV* CURVES IN FIGURES 51 AND 52. REDOX SHUTTLE: I_3^-/I^-; *JV* SCAN RATE: 20 mV s^{-1}; INCIDENT LIGHT INTENSITY: 0.1 W cm^{-2}. ALL SAMPLES HAVE BEEN OBTAINED VIA PLASMA ASSISTED SINTERING OF SPRAY-DEPOSITED NiO NANOPARTICLES SLURRY HEATED IN MICROWAVE CHAMBER. [33] SAMPLES 1, 2 AND 3 REFER TO THE SAMPLES OBTAINED VIA NiO SLURRY SPRAY-DEPOSITION ONTO UNHEATED FTO SUBSTRATE, [76] VIA NiO SLURRY SPRAY-DEPOSITION ONTO HEATED FTO SUBSTRATE, AND VIA NiO SLURRY SPRAY-DEPOSITION ONTO PLASMA TREATED AND HEATED FTO SUBSTRATE, RESPECTIVELY. [32] FTO SUBSTRATE WAS HEATED IN THE TEMPERATURE RANGE 60-75 °C DURING SPRAY DEPOSITION OF SAMPLES 2 AND 3.

NiO type	*l* / μm	η / %	V_{OC} / V	- J_{SC} / mA cm^{-2}	FF	*IPCE* / %
1(1st test)	**0.6**	**0.014**	**0.130**	**0.290**	**0.370**	-
1(2nd test)	**0.6**	**0.015**	**0.130**	**0.330**	**0.360**	-
1(1st test)	**1-2**	**0.045**	**0.120**	**1.050**	**0.360**	-
1(2nd test)	**1-2**	**0.028**	**0.095**	**0.820**	**0.358**	**3**
1(3rd test)	**1-2**	**0.025**	**0.095**	**0.821**	**0.319**	**7**
1(1st test)	**5-6**	**0.030**	**0.100**	**0.787**	**0.380**	**11**
1(2nd test)	**5-6**	**0.029**	**0.095**	**0.869**	**0.357**	**10**
2(1st test)	**1-2**	**0.035**	**0.105**	**0.872**	**0.384**	**8**
2(2nd test)	**1-2**	**0.033**	**0.105**	**0.830**	**0.380**	**6**
2(1st test)	**3-4**	**0.039**	**0.095**	**1.016**	**0.400**	**8**
2(2nd test)	**3-4**	**0.037**	**0.080**	**1.161**	**0.393**	**5**
3(1st test)	**2-3**	**0.022**	**0.110**	**0.594**	**0.335**	**9**
3(2nd test)	**2-3**	**0.011**	**0.060**	**0.719**	**0.266**	**4**

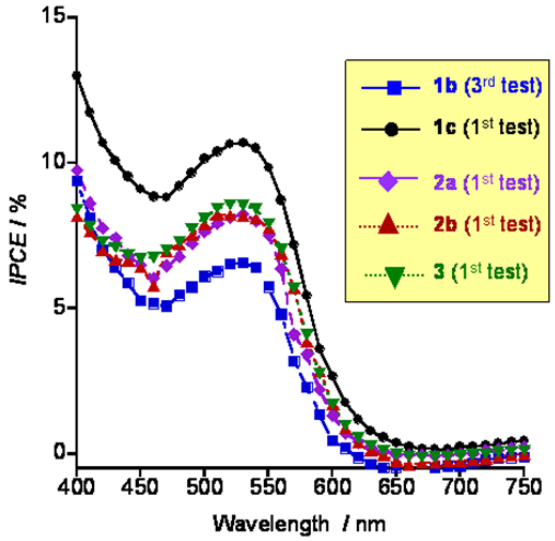

FIGURE 53. IPCE SPECTRA OF THE *P*-DSCS UTILIZING NiO PHOTOCATHODES OF THREE DIFFERENT TYPES (SEE TABLE 1). NiO FILM THICKNESS VALUES ARE: 1-2 μm (SAMPLES 1B AND 2A); 2-3 μm (SAMPLE 3); 3-4 μm (SAMPLE 2B); 5-6 μm (SAMPLE 1C). REDOX SHUTTLE: I_3^-/I^- ; ACTIVE AREA OF THE DEVICE: 0.5-0.7 cm^2; SENSITIZER: ERYTHROSINE b. SAMPLE DESCRIPTION IS GIVEN IN TABLE 2 (SEE ABOVE). ADAPTED FROM REF. 32.

More promising results have been obtained when the sensitizer of the NiO based p-DSCs was P1 (**Figure 8**), [25] which actually represents one of the few colorants appositely designed for *p*-DSCs and it is not simply an adaptation of an organic dye originally used in TiO_2 based *n*-DSCs. [56, 76] The most important progresses of P1 based *p*-DSCs were achieved in terms of efficiency increase with respect to erythrosine dye-benchmark being quite common to reach values of η not inferior to 0.10 % (**Table 3**). Again, the parameter of the *p*-DSC most poorly affected by the ameliorated colorant P1 was the fill factor which ranged quite regularly between 0.31 and 0.35.

TABLE 3. LIST OF PARAMETERS OBTAINED FROM THE *JV* CURVES IN FIGURES 54 AND 55(*VIDE INFRA*) OF THE *p*-DSCs UTILIZING DIFFERENTLY PREPARED NiO PHOTOCATHODES. SENSITIZER: P1; REDOX SHUTTLE: I_3^-/I^-; *JV* SCAN RATE: 20 mV s^{-1}; SAMPLE AREA: 0.7 cm^2; INCIDENT LIGHT INTENSITY: 0.1 W cm^{-2}. SAMPLES 1-3 ARE OF TYPES REPORTED IN THE CAPTION OF TABLE 2. SAMPLE 4 HAS BEEN PREPARED WITH CONVENTIONAL SINTERING.[19,56]

NiO_x sample	***l* / μm**	***η* / %**	**V_{OC} / V**	**- J_{SC} / mA cm^{-2}**	**FF**	*IPCE / %*
1	0.6	0.099	0.170	1.890	0.310	-
1(1st test)	1-2	0.113	0.130	2.790	0.320	-
1(2nd test)	1-2	0.048	0.080	1.760	0.340	22
1(3rd test)	1-2	0.076	0.090	2.600	0.326	24
1(4th test)	1-2	0.061	0.085	2.070	0.349	19
1(1st test)	5-6	0.065	0.090	2.200	0.330	22
1(2nd test)	5-6	0.072	0.100	2.170	0.330	27
1(3rd test)	5-6	0.066	0.090	2.230	0.330	22
2(1st test)	1-2	0.066	0.075	2.570	0.341	20
2(2nd test)	1-2	0.080	0.085	2.770	0.340	25
2(3rd test)	1-2	0.076	0.080	2.940	0.322	26
2(1st test)	3-4	0.071	0.075	2.930	0.323	29
2(2nd test)	3-4	0.085	0.080	3.200	0.333	25
2(3rd test)	3-4	0.079	0.080	2.960	0.332	24
3(1st test)	2-3	0.046	0.080	1.630	0.354	14
3(2nd test)	2-3	0.084	0.090	2.810	0.332	22
3(3rd test)	2-3	0.065	0.085	2.370	0.321	14
4	0.6	0.037	0.160	0.680	0.330	-

In terms of spectral quantum efficiency, P1 induces IPCE maxima of about 30 % in the spectral interval 400-600 nm (**Figure 56**).[19, 41, 55] When the dye of nanostructured NiO augments its effectiveness, the EIS profile of the corresponding *p*-DSC is characterized by a very low resistance of recombination (amplitude of the second semicircle in the EIS profile, **Figure 57**). This finding is directly related to the higher surface concentration of photoinjected holes at the condition of open circuit potential when more efficacious dye sensitizers are employed. [56 and references therein] Such a finding reveals the non-obvious relationship of inverse proportionality between overall *p*-DSC efficiency and recombination resistance due to the bimolecular nature of the recombination process (Eq. 9).

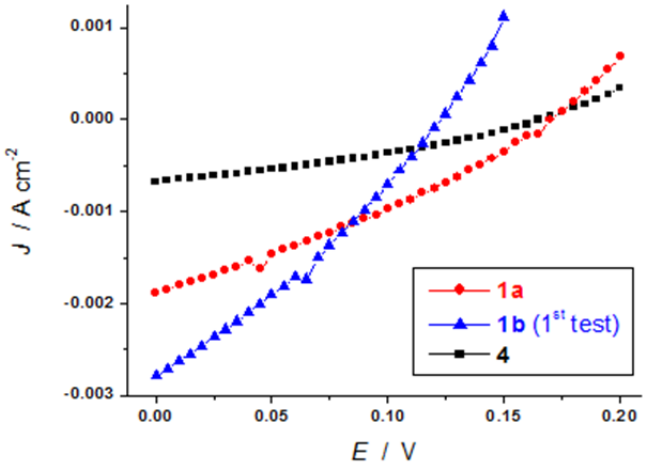

FIGURE 54. *JV* CURVES FOR DIFFERENT NiO SAMPLES (1 AND 4) IN I_3^-/I^- BASED CATHODIC DSCs. DEVICE AREA: 0.5-0.7 cm^2; SENSITISER: P1; SCAN RATE: 20 mV s^{-1}; INCIDENT LIGHT POWER: 0.1 W cm^{-2}. NiO FILMS HAVE THICKNESS VALUES: 0.6 μm (SAMPLES 1a AND 4); 1-2 μm (SAMPLE 1b). THE METHODS OF SAMPLES DEPOSITION AND PREPARATION ARE GIVEN IN THE CAPTIONS OF TABLES 2 AND 3. ADAPTED FROM REF. 19.

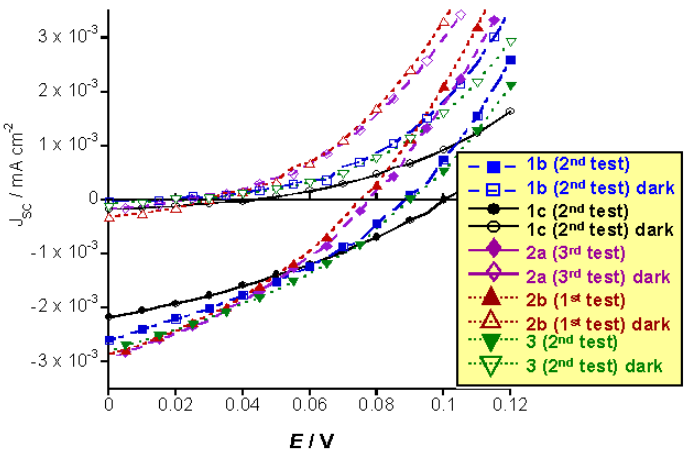

FIGURE 55. *JV* CURVES FOR DIFFERENT NiO SAMPLES (**1**-**3**) IN I_3^-/I^- BASED CATHODIC DSCs. DEVICE AREA: 0.5-0.7 cm^2; SENSITISER: P1; SCAN RATE: 20 mV s^{-1}; INCIDENT LIGHT POWER: 0.1 W cm^{-2}. NiO FILMS HAVE THICKNESS VALUES: 1-2 μm (SAMPLES **1b** AND **2a**); 2-3 μm (SAMPLE **3**); 3-4 μm (SAMPLE **2b**); 5-6 μm (SAMPLE **1c**). SAMPLES DESCRIPTION IS REPORTED IN THE CAPTION OF TABLE 2. ADAPTED FROM REF. 19.

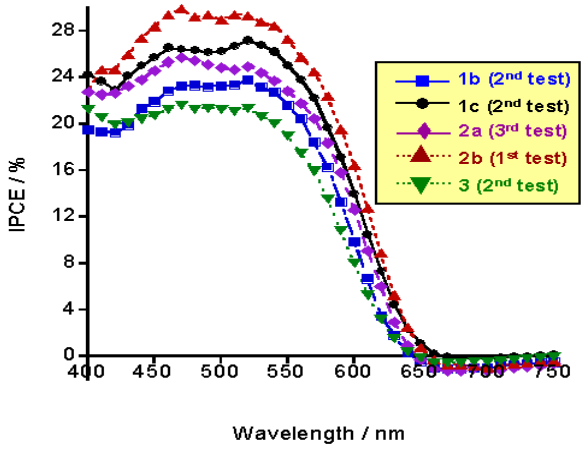

FIGURE 56. IPCE CURVES FOR THE *p*-DSCs UTILIZING DIFFERENTLY PREPARED NAN-OPOROUS NiO PHOTOCATHODES. SENSITIZER: P1; REDOX SHUTTLE: I_3^-/I^-; SAMPLE AREA: 0.7 cm^2. SAMPLE DESCRIPTION IS GIVEN IN TABLE 2. NiO FILMS HAVE THICKNESS VALUES IN THE RANGES: 1-2 μm (SAMPLES 1b AND 2a); 2-3 μm (SAMPLE 3); 3-4 μm (SAMPLE 2b); 5-6 μm (SAMPLE 1c). ADAPTED FROM REF. 19.

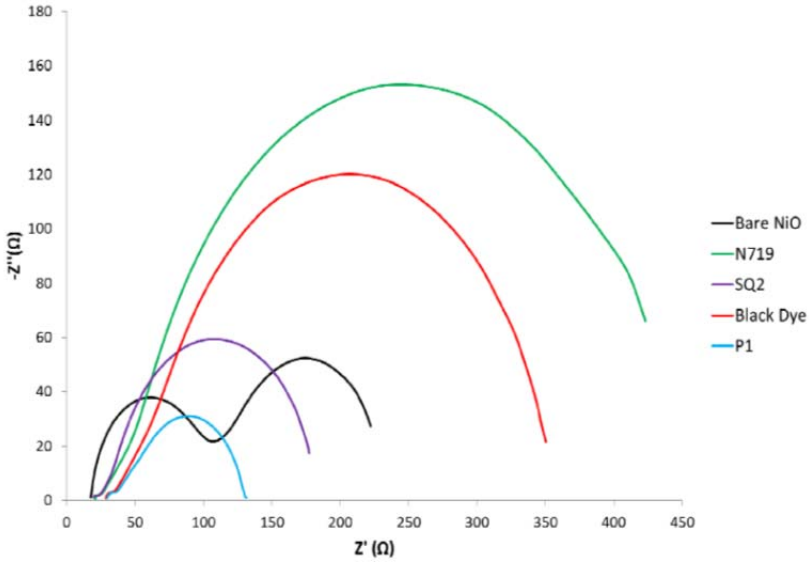

FIGURE 57. EIS PROFILES OF THE *p*-DSCs USING NANOSTRUCTURED NiO OF TYPE **2** (SEE CAPTION OF TABLE 2) IN THE BARE AND THE SENSITIZED STATES WITH N719, A COMMERCIAL SQUARAINE (SQ2), P1 AND BLACK DYE AS COLORANTS. CELLS HAVE BEEN POLARIZED AT THEIR V_{OC} AND IRRADIATED WITH ONE SUN OF ILLUMINATION. ADAPTED FROM REF.56.

Conclusions

The present contribution on nanostructured *p*-type semiconducting materials for application in solar energy conversion has first reviewed the general characteristic of a nanostructured semiconductor and the implications of that in the utilization of this type of materials in photoelectrochemical devices like dye-sensitized solar cells (DSCs). In particular, in the framework of DSCs it has been recognized the importance of the characteristic of mesoporosity in nanostructured electrodes for three main reasons: i) acceleration of surface dependent photoelectrochemical processes; ii) the possibility of loading high amounts of dye-sensitizer; iii) achievement of high optical transmission for the photoelectrodes in their bare unsensitized state. In confining the interest towards the sole class of nanostructured *p*-type semiconductors for the application of cathodic DSCs, it has been widely recognized the choice of nickel oxide (NiO or, more generally, with formula NiO_x in case of the non-stoichiometric oxide) as the material *par excellence* for this type of photoelectrochemical devices. This is because nickel oxide can be prepared and deposited in a variety of nanostructures with either elongated, spherical or spongy morphology without losing or affecting considerably the intrinsic electrical conductivity and electron transfer properties with respect to the bulk version. Moreover, thickness modulation as well as NiO film adhesion on technical substrates are aspects now under full control in most of the deposition methods so far adopted and developed. Other factors crucial for NiO performance in DSC are represented by the degree of crystallinity, nanostructure size and dimensionality, and chemical purity of the phase(s) composing the metal oxide electrode. The recent progresses on the synthetic procedures of NiO have led to the full control of these factors as well. The review shows also that nanostructured nickel oxide is by far from being an ideal cathodic material for *p*-DSCs for several reasons: high optical absorbance in the bare state; intrinsic photoelectrochemical activity which might get in conflict with the process of external photoinjection dictated by the anchored sensitizer; the presence of surface defects which might accelerate recombination processes; lack of a very efficacious dye purposely designed for the optimized sensitization of NiO; intrinsic electrocatalytic activity of of NiO which can lead to charge trapping; charge storage properties and capacitive behaviour of NiO which limit kinetically the process of charge transport through the oxide itself. In terms of solar cell performance, these limitations produce generally poor overall efficiencies (generally lower than 1.5 %) and low fill factor (systematically less than 0.5) in the corresponding *p*-DSC devices utilizing NiO photocathodes. The utilization of nanostructured *p*-type electrodes in the definition and assembly of DSC with tandem configuration, i.e. with both photoactive electrodes, has been discussed.

REFERENCES

[1] A. Hagfeldt, G. Boschloo, L. Sun, L. Kloo, H. Pettersson, Chem. Rev. 2010, 110, 6595-6663

[2] H. Gerischer, M.E. Michel-Beyerle, F. Rebentrost, H. Tributsch, Electrochim. Acta 1968, 13, 1509-1515

[3] F. Gutmann, L.E. Lyons, Organic Semiconductors, John Wiley & Sons, New York: 1967

[4] A. Hagfeldt, M. Grätzel, Chem. Rev. 1995, 95, 49-68

[5] B. O'Regan, M. Grätzel, Nature 1991, 353, 737-740

[6] S. Ito, T.N. Murakami, P. Comte, P. Liska, C. Grätzel, M.K. Nazeeruddin, M. Grätzel, Thin Solid Films 2008, 516, 4613-4619

[7] A. Yella, H.W. Lee, H.N. Tsao, C. Yi, A.K. Chandiran, M.K. Nazeeruddin, E.W.G. Diau, C.Y. Yeh, S.M. Zakeeruddin, M. Grätzel, Science 2011, 334, 629-634

[8] S. Mathew, A. Yella, P. Gao, R. Humphry-Baker, B.F.E. Curchod, N. Ashari-Astani, I. Tavernelli, U. Rothlisberger, M.K. Nazeeruddin, M. Grätzel, Nature Chem. 2014, 6, 242-247

[9] L. Brus, J. Phys. Chem, 1986, 90, 2555-2560

[10] L.A. Harris, R.H. Wilson, Ann. Rev. Mater. Sci. 1978, 8, 99-134

[11] N. Mott, Conduction in Non-crystalline Materials, Oxford Science Publication, Oxford, 1987

[12] J. Bisquert, A. Zaban, P. Salvador, J. Phys. Chem. B 2002, 106, 8774-8782

[13] H.M. Rosenberg, The Solid State (Oxford Physics Series), Oxford University Press, Oxford: 1988

[14] J. Bisquert, Phys. Chem.. Chem. Phys. 2003, 5, 5360-5364

[15] W.P. Gomes, F. Cardon, Prog. Surf. Sci. 1982, 12, 155-216

[16] J. He, H. Lindström, A. Hagfeldt, S.E. Lindquist, Solar Energy Mater. Solar Cells 2000, 62, 265-273

[17] S. Sumikura, S. Mori, S. Shimizu, H. Usami, E. Suzuki, J. Photochem. Photobiol. A 2008, 199, 1-7

[18] M. Awais, D.P. Dowling, M. Rahman, J.G. Vos, F. Decker, D. Dini, J. Appl. Electrochem. 2013, 43, 191-197

[19] (a) E.A. Gibson, M. Awais, D. Dini, D.P. Dowling, M.T. Pryce, J.G. Vos, G. Boschloo, A. Hagfeldt, Phys. Chem. Chem. Phys. 2013, 15, 2411-2420; (b) M. Shinde, N. Qureshi, S. Rane, U. Mulik, D. Amalnerkar, Phys. Chem. Commun. 2015, 2, 1-9

[20] Semiconductor Electrodes, Studies in Physical and Theoretical Chemistry (H. O'Finklea ed.), Elsevier: Amsterdam, 1988

[21] I. Venditti, N. Barbero, M.V. Russo, A. Di Carlo, F. Decker, I. Fratoddi, C. Barolo, D. Dini, Mater. Res. Express 2014, 1, 015040/1-18

[22] A. Hagfeldt, U.B. Cappel, G. Boschloo, L. Sun, L. Kloo, H. Pettersson, E.A. Gibson: 'Dye Sensitized Photoelectrochemical Cells', in Practical Handbook of Photovoltaics: Fundamentals and Applications, 2nd Ed., Elsevier, 2012. Eds. A. McEvoy, T. Markvart and L. Castaner. Pages 479-542.

[23] B.E. Hardin, H.J. Snaith, Michael, D. McGehee, Nature Photonics 2012, 6, 162-169

[24] A. Nattestad, M. Ferguson, R. Kerr, Y.B. Cheng, U. Bach, Nanotechnology 2008, 19, 295304/1-9

[25] P. Qin, H. Zhu, T. Edvinsson, G. Boschloo, A. Hagfeldt, L. Sun, J. Am. Chem. Soc. 2008, 130, 8570-8571

[26] G. Naponiello, I. Venditti, V. Zardetto, D. Saccone, A. Di Carlo, I. Fratoddi, C. Barolo, D. Dini, Appl. Surf. Sci. 2015, 356, 911-920

[27] A. Nakasa, H. Usami, S. Sumikura, S. Hasegawa, T. Koyama, E. Suzuki, Chem. Lett. 2005, 34, 500-501

[28] A. Nattestad, A. J. Mozer, M.K.R. Fischer, Y.B. Cheng, A. Mishra, P. Bäuerle, U. Bach, Nature Mater. 2010, 9, 31-35

[29] C.J. Wood, G. H. Summers, E.A. Gibson, Chem. Commun. 2015, 51, 3915-3918

[30] M. Weidelener, A. Mishra, A. Nattestad, S. Powar, A.J. Mozer, E. Mena-Osteritz, Y.B. Cheng, U. Bach, P. Bäuerle, J. Mater. Chem. 2012, 22, 7366-7379

[31] D. Dini, Y. Halpin, J.G. Vos, E.A. Gibson, Coord. Chem. Rev. 2015, 304-305, 179-201

[32] M. Awais, E. Gibson, J.G. Vos, D.P. Dowling, A. Hagfeldt, D. Dini, ChemElectroChem 2014, 2, 384-391

[33] M. Awais, M. Rahman, J.M. Don MacElroy, D. Dini, J.G. Vos, D.P. Dowling, Surf. Sci. Techn. 2011, 205, S245-S249

[34] J.F. Lefebvre, X.Z. Sun, J.A. Calladine, M.W. George, E.A. Gibson Chem. Commun. 2014, 50, 5258-5260

[35] C.J. Wood, K.C.D. Robson, P.I.P. Elliott, C.P. Berlinguette, E.A. Gibson, RSC Adv. 2014, 4, 5782-5791

[36] D. Ameline, S. Diring, Y. Farre, Y. Pellegrin, G. Naponiello, E. Blart, B. Charrier, D. Dini, D. Jacquemin, F. Odobel, RSC Adv. 2015, 5, 85530-85539

[37] W. Shockley, H.J. Queisser, J. Appl. Phys. 1961, 32, 510-519

[38] C.H. Henry, J. Appl. Phys. 1980, 51, 4494-4500

[39] P.K. Nayak, G. Garcia-Belmonte, A. Kahn, J. Bisquert, D. Cahen, Energy Environ. Sci. 2012, 5, 6022-6039

[40] M.A. Green, Third Generation Photovoltaics: Advanced Solar Energy Conversion; Springer-Verlag: Berlin, Heidelberg, 2003

[41] E.A. Gibson, A.L. Smeigh, L. Le Pleux, J. Fortage, G. Boschloo, E. Blart, L. Hammarström, Angew. Chem. Inter. Ed. 2009, 48, 4402-4405

[42] M. Awais, D.P. Dowling, F. Decker, D. Dini, SpringerPlus 2015, 4, 564/1-24

[43] J. Bisquert, F. Fabregat-Santiago, Dye-sensitized solar cells, ed. K. Kalyanasundaram, CRC Press: Boca Raton, 2010; p.457-554

[44] J. Bisquert, Phys. Chem. Chem. Phys. 2008, 10, 49-72

[45] S.M. Sze, Physics of Semiconductor Devices, Wiley-Interscience: New York, 1969

[46] G. Boschloo, A. Hagfeldt, Acc. Chem. Res. 2009, 42, 1819-1826

[47] J. Cong, X. Yang, L. Kloo, L. Sun, Energy Environ. Sci. 2012, 2, 9180-9194

[48] H. Wang, Z. Sun, Y. Zhang, M. Liang, D. Jia, S. Xue, J. Phys. Chem. C 2014, 118, 60-70

[49] B. Gregg, Coord. Chem. Rev. 2004, 248, 1215-1224

[50] Dye-Sensitized solar cells (Fundamental Sciences Series, Chemistry), ed. K. Kalyanasundaram, Lausanne: EPFL Press, CRC, 2010

[51] S. Powar, T. Daeneke, M.T. Ma, D. Fu, N.W. Duffy, G. Götz, Martin Weidelener, A. Mishra, P. Bäuerle, L. Spiccia, U. Bach, Angew. Chemie. Int. Ed. 2013, 52, 602-605

[52] S. Powar, Q. Wu, M. Weidelener, A. Nattestad, Z. Hu, A. Mishra, P. Bäuerle, L. Spiccia, Y.B. Cheng, U. Bach, Energy Environ. Sci. 2012, 5, 8896-8900

[53] T. Daeneke, Z. Yu, G.P. Lee, D. Fu, N.W. Duffy, S. Makuta, Y. Tachibana, L. Spiccia, A. Mishra, P. Bäuerle, U. Bach, Adv. Energy Mater. 2015, 5, 1401387/1-11

[54] M. Bräutigam, P. Weyell, T. Rudolph, J. Dellith, S. Krieck, H. Schmalz, F.H. Schacher, B. Dietzek, J. Mater. Chem. A 2014, 2, 6158-6166

[55] L. Li, E. A. Gibson, P. Qin, G. Boschloo, M. Gorlov, A. Hagfeldt, L. Sun, Adv. Mater. 2010, 22, 1759-1762

[56] S. Sheehan, G. Naponiello, F. Odobel, D.P. Dowling, A. Di Carlo, D. Dini, J. Solid State Electrochem. 2015, 19, 975-986

[57] A. Burke, S. Ito, H. Snaith, U. Bach, J. Kwiatkowski, M. Gratzel, Nano Lett. 2008, 8, 977-981

[58] W. Estrada, A.M. Andersson, C.G. Granqvist, A. Gorenstein, F. Decker, J. Mater. Res. 1991, 6, 1715-1719

[59] A.G. Marrani, V. Novelli, S. Sheehan, D.P. Dowling, D. Dini, ACS Appl. Mater. Interfaces 2014, 6, 143-152

[60] S. Nandy, U.N. Maiti, C.K. Ghosh, K.K. Chattopadhyay, J. Phys. Condens. Matter 2009, 21, 115804/1-7

[61] M. Awais, D.P. Dowling, F. Decker, D. Dini, Adv. Condens. Matter Phys. 2015, 2015, 186375/1-18

[62] M. Zannotti, C.J. Wood, G.H. Summers, L.A. Stevens, M.R. Hall, C.E. Snape, R. Giovannetti, E.A. Gibson, ACS Appl. Mater. Interfaces 2015, 7, 24556-24565

[63] H.T. Wang, D.K. Mishra, P. Chen, J.M. Ting, J. Alloys Compounds 2014, 584, 142-147

[64] L. D'Amario, G. Boschloo, A. Hagfeldt , L. Hammarstrom, J. Phys. Chem. C 2014, 118, 19556-19564

[65] T. Dutta, P. Gupta, A. Gupta, J. Narayan, J. Appl. Phys. 2010, 108, 083715/1-7

[66] M.S. Wu, M.J. Wang, Chem. Commun. 2010, 46, 6968-6970

[67] J. Nepal, S.S. Mottaghian, M. Biesecker, M.F. Baroughi, Appl. Phys. Lett. 2013, 102, 203503/1-4

[68] L. Peter, J. Electroanal. Chem. 2007, 599, 233-240

[69] L. Bertoluzzi, S. Ma, Phys. Chem. Chem. Phys. 2013, 15, 4283-4285

[70] J. Yang, M. Cho, Y. Lee, Sensors Actuat. B 2016, 222, 674-681

[71] R.T. Wen, C.G. Granqvist, G.A. Niklasson, Appl. Phys. Lett. 2014, 105, 163502/1-4

[72] M.S. Balogun, W.T. Qiu, Y. Luo, Y.C. Huang, H. Yang, M.Y. Li, M.H. Yu, C.L. Liang, P.P. Fang, P. Liu, Y.X. Tong, ChemElectroChem 2015, 2, 1243-1248

[73] M. Awais, D. Dini, J.M. Don MacElroy, Y. Halpin, J.G. Vos, D.P. Dowling, J. Electroanal. Chem. 2013, 689, 185-192

[74] F. Decker, S. Passerini, R. Pileggi, B. Scrosati, Electrochim. Acta 1992, 37, 1033-1038

[75] G. Boschloo, A. Hagfeldt, J. Phys. Chem. B 2001, 105, 3039-3044

[76] V. Novelli, M. Awais, D.P. Dowling, D. Dini, Am. J. Anal. Chem. 2015, 6, 176-187

[77] Alessandro Rossi, Master Thesis (University of Rome LA SAPIENZA, 2015). Title: *Electrochemical response of nanostructured electroactive oxides in various electrolytes for energy conversion devices*

[78] F. Vera, R. Schrebler, E. Muñoz, C. Suarez, P. Cury, H. Gómez, R. Córdova, R.E. Marotti, E. Dalchiele, Thin Solid Films 2005, 490, 182-188

[79] J. He, H. Lindström, A. Hagfeldt, S.E. Lindquist, J. Phys. Chem. B 1999, 103, 8940-8943

[80] V.P.S. Perera, P.K.D.D.P. Pitigala, M.K.I. Senevirathne, K. Tennakone, Solar Energy Mater, Solar Cells 2005, 85, 91-98

[81] Y. Pellegrin, L. Le Pleux, E. Blart, A. Renaud, B. Chavillon, N. Szuwarski, M.Boujtita, L. Cario, S. Jobic, D. Jacquemin, F. Odobel, J. Photochem. Photobio. A, 2011, 219, 235–242

[82] L. Le Pleux, A.L. Smeigh, E. Gibson, Y. Pellegrin, E. Blart, G. Boschloo, A. Hagfeldt, L. Hammarström, F. Odobel, Energy Environ. Sci. 2011, 4, 2075-2084

[83] A. Renaud, B. Chavillon, L. Le Pleux, Y. Pellegrin, E. Blart, M. Boujtita, D. Jacquemin, F. Odobel, Chem. Commun. 2013, 49, 8018-8020

[84] X.L. Zhang, F. Huang, A. Nattestad, K. Wang, D. Fu, A. Mishra, P. Bäuerle, U. Bach, Y.B. Cheng, Chem. Commun. 2011, 47, 4808-4810

[85] X.L. Zhang, Z. Zhang, F. Huang, P. Bäuerle, U. Bach, Y.B. Cheng, J. Mater. Chem. 2012, 22, 7005-7009

[86] L. Lepleux, B. Chavillon,Y. Pellegrin, E. Blart, L. Cario, S. Jobic, F. Odobel, Inorg. Chem. 2009, 48, 8245-8250